View metadata, citation and similar papers at core.ac.uk
brought to you by CORE
provided by UT Digital Repository

A&A 550, A122 (2013)
DOI: 10.1051/0004-6361/201219949
© ESO 2013

Astronomy & Astrophysics

First stars

XVI. HST/STIS abundances of heavy elements in the uranium-rich metal-poor star CS 31082-001⋆,⋆⋆

C. Siqueira Mello Jr.[1,2], M. Spite[2], B. Barbuy[1], F. Spite[2], E. Caffau[3,2], V. Hill[4], S. Wanajo[5], F. Primas[6], B. Plez[7], R. Cayrel[8], J. Andersen[9,10], B. Nordström[9], C. Sneden[11], T. C. Beers[12,13], P. Bonifacio[2], P. François[8], and P. Molaro[14]

[1] Universidade de São Paulo, IAG, Rua do Matão 1226, Cidade Universitária, 05508-900 São Paulo, Brazil
e-mail: cesar.mello@usp.br
[2] GEPI, Observatoire de Paris, CNRS, UMR 8111, 92195 Meudon Cedex, France
[3] Zentrum für Astronomie der Universität Heidelberg, Landessternwarte, Königstuhl 12, 69117 Heidelberg, Germany
[4] Laboratoire Lagrange, UMR 7293, Université de Nice Sophia-Antipolis, CNRS, Observatoire de la Côte d'Azur, 06300 Nice, France
[5] National Astronomical Observatory of Japan, 2-21-1 Osawa, Mitaka, 181-8588 Tokyo, Japan
[6] European Southern Observatory, Karl Schwarzschild Strasse 2, 85748 Garching bei München, Germany
[7] LUPM, CNRS, UMR 5299, Université de Montpellier II, 34095 Montpellier Cedex 05, France
[8] GEPI, Observatoire de Paris, CNRS, UMR 8111, 61 Av. de l'Observatoire, 75014 Paris, France
[9] The Niels Bohr Institute, Juliane Maries Vej 30, 2100 Copenhagen, Denmark
[10] Nordic Optical Telescope, Apartado 474, 38700 Santa Cruz de La Palma, Spain
[11] University of Texas at Austin, Department of Astronomy, Austin, TX 78712, USA
[12] National Optical Astronomy Observatory, Tucson, MI 85719, USA
[13] Michigan State University, Department of Physics & Astronomy, and JINA, Joinst Institute for Nuclear Physics, East Lansing, MI 48824, USA
[14] INAF – Osservatorio Astronomico di Trieste, via Tiepolo 11, 34143 Trieste, Italy

Received 5 July 2012 / Accepted 8 November 2012

ABSTRACT

Context. The origin and site(s) of the r-process nucleosynthesis is(are) still not known with certainty, but complete, detailed r-element abundances offer our best clues. The few extremely metal-poor (EMP) stars with large r-element excesses allow us to study the r-process signatures in great detail, with minimal interference from later stages of Galactic evolution. CS 31082-001 is an outstanding example of the information that can be gathered from these exceptional stars.
Aims. Here we aim to complement our previous abundance determinations for third-peak r-process elements with new and improved results for elements of the first and second r-process peaks from near-UV HST/STIS and optical UVES spectra. These results should provide new insight into the nucleosynthesis of the elements beyond iron.
Methods. The spectra were analyzed by a consistent approach based on an OSMARCS LTE model atmosphere and the *Turbospectrum* spectrum synthesis code to derive abundances of heavy elements in CS 31082-001, and using updated oscillator strengths from the recent literature. Synthetic spectra were computed for all lines of the elements of interest to check for proper line intensities and possible blends in these crowded spectra. Our new abundances were combined with the best previous results to provide reliable mean abundances for the first and second-peak r-process elements.
Results. We present new abundances for 23 neutron-capture elements, 6 of which – Ge, Mo, Lu, Ta, W, and Re – have not been reported before. This makes CS 31082-001 the most completely studied r-II star, with abundances for a total of 37 neutron-capture elements. We also present the first NLTE+3D abundance of lead in this star, further constraining the nature of the r-process.

Key words. stars: abundances – stars: Population II – Galaxy: halo – stars: individual: BPS CS 31082-001

1. Introduction

The origin of the elements beyond the iron peak is described in terms of the two major mechanisms of neutron capture, the s-process and the r-process. The s-process occurs at a slower rate than the half-life of beta decay, while the r-process occurs at a rapid rate, shorter than the beta decay intervention timescale (Burbidge et al. 1957). The difference in timescale is associated with different neutron fluxes, boosting the seed nuclei into heavier nuclei; as a consequence, completely different astrophysical sites are needed for these mechanisms. Notwithstanding, the site(s) of r-element production is(are) still not known with certainty (e.g. Wanajo & Ishimaru 2006; Kratz et al. 2007; Thielemann et al. 2010).

Popular models involve high-entropy neutrino-driven winds of neutron-rich matter, which build up heavy nuclei near the neutrino sphere of a core-collapse supernova (Woosley et al. 1994; Wanajo 2007, and references therein). Studies of Galactic chemical evolution suggest that core-collapse supernovae, in particular near the low-mass end (8−10 $M_{\odot}$), are the dominant source of r-process elements (e.g. Mathews & Cowan 1990; Ishimaru & Wanajo 1999).

⋆ Based on observations made with the NASA/ESA *Hubble* Space Telescope (HST) through the Space Telescope Science Institute, operated by the Association of Universities for Research in Astronomy, Inc., under NASA contract NAS5-26555; and with the ESO Very Large Telescope at Paranal Observatory, Chile; Progr. ID 165.N-0276.
⋆⋆ Appendix A is available in electronic form at http://www.aanda.org

However, hydrodynamical simulations with accurate neutrino transport have shown that neutrino winds are in fact proton-rich (Fischer et al. 2010; Hüdepohl et al. 2010) or only slightly neutron-rich (Martínez-Pinedo et al. 2012; Roberts 2012; Roberts et al. 2012), and not very neutron-rich, as found in some older simulations (Woosley et al. 1994). Since hydrodynamical simulations still encounter difficulties reproducing the astrophysical conditions of the process, the neutrino wind scenario for the origin of the heavy r-process elements is in doubt.

Neutron-rich ejecta from neutron star-neutron star (NS-NS) or black hole-neutron star (BH-NS) binary mergers have been suggested as plausible alternative astrophysical sites of the main r-process (Lattimer et al. 1977; Meyer 1989; Freiburghaus et al. 1999; Surman et al. 2008; Goriely et al. 2011; Wanajo et al. 2011; Korobkin et al. 2012). However, the time scales may not be appropriate for such extremely old and metal-poor stars as CS 31082-001.

As recently discussed by Peterson (2011), the origin of the lightest trans-Fe elements, from gallium through cadmium (Z = 31 to 48), appears even more complex. These elements have been attributed in varying degrees to a weak s-process (Clayton 1968; Käppeler et al. 1989), to a so-called light element primary process (LEPP; Travaglio et al. 2004), such as a weak r-process (Wanajo & Ishimaru 2006; Farouqi et al. 2010; Wanajo et al. 2011), and/or to the νp-process in core-collapse supernovae (Fröhlich et al. 2006; Pruet et al. 2006; Wanajo 2006; Arcones & Montes 2011).

Detailed abundances of the elements produced by r-process nucleosynthesis in various circumstances are the key observational clues to the nature of this mechanism. The clearest picture is obtained by considering the products of heavy-element in the first generations of stars, as recorded in the low-mass extremely metal-poor (EMP) Galactic halo stars that survive until today. Dramatic excesses of neutron-capture elements are present in some of these stars, and provide constraints on the synthesis process(es), the astrophysical site(s) for the r-process and the nature of the stellar generations in the early Galaxy.

CS 31082-001, CS 22892-052, and HE 1523-0901 are the most prominent among the only 12 known extremely r-element enhanced EMP (r-II)[1] giant stars, and their abundance patterns have been studied in great detail. Recently, Barbuy et al. (2011) performed a complete analysis of third-peak r-element and actinide abundances in CS 31082-001 using near-UV HST/STIS spectra.

In the present paper, we analyze the first- and second-peak r-elements from near-UV lines in the same STIS spectra and in a UVES/VLT spectrum centered at 340 nm. The first peak comprises the elements with $38 \leq Z \leq 48$, while the second peak ($56 \leq Z \leq 72$) includes the lanthanides ($57 \leq Z \leq 71$). These elements can be produced in both the slow and rapid neutron-capture processes, but Truran (1981) showed that in EMP stars these elements are predominantly due to the r-process, because intermediate-mass AGB stars had no time to enrich the matter before the formation of the observed EMP stars.

It is worth noting here that, while some EMP stars are found to be strongly enhanced in carbon and s-process elements, commonly ascribed to later pollution from a former AGB binary companion, Hansen et al. (2011) have recently shown that the occasional strong r-process enhancements in EMP giants – including CS 31082-001 itself – are unrelated to any binary companions, but rather were imprinted on the material from which these stars first formed in the early ISM.

[1] Following the classification from Beers & Christlieb (2005).

This paper is organized as follows. Section 2 describes the observations and data reduction; Sect. 3 summarizes our abundance determination methods as well as the adopted abundance for each element; Sect. 4 discusses the results in the context of r-process models; and Sect. 5 summarises our conclusions.

2. Observations

CS 31082-001 was observed with the Space Telescope Imaging Spectrograph (STIS) in the near-UV (program ID 9359; PI: Cayrel). STIS spectroscopic mode E230M combines an échelle grating with an NUV-MAMA detector to obtain spectra in the wavelength range 1575−3100 Å, at a resolution of R = 30 000. More detail is given in Barbuy et al. (2011).

To complement these observations, we used the mean of three UVES spectra centered at 340 nm, obtained at the VLT in October 2001 in the course of the large program "First Stars". In the common range of wavelengths (300 nm < λ < 307 nm), the co-added spectrum has a higher resolution (R = 75 000) than the HST spectrum, and a signal-to-noise ratio of about 20 at 300 nm and 100 at 340 nm, and it was not used by Hill et al. (2002). The reduction of these spectra was performed using the UVES context within MIDAS: bias subtraction, fit and subtraction of the interorder background from the object, and flat-field images. The wavelength calibration was performed on Th-Ar lamp frames and used to build a co-added spectrum. Since this spectrum was obtained after those used by Hill et al. (2002), we refer to this as our "new" UVES spectrum.

3. Abundance determination

The present abundance determinations are based on a recent version of the OSMARCS 1D local thermodynamic equilibrium (LTE) model atmospheres (Gustafsson et al. 1975; Plez et al. 1992; Asplund et al. 1997), updated for cool stars (Gustafsson et al. 2003, 2008). Like Hill et al. (2002) and Barbuy et al. (2011), we used a consistent approach based on the spectrum synthesis code Turbospectrum (Alvarez & Plez 1998), which includes a full chemical equilibrium and Van der Waals collisional broadening by H, He, and H_2, following Anstee & O'Mara (1995), Barklem & O'Mara (1997), and Barklem et al. (1998). The code also properly accounts for scattering in the continuum, an important effect in the UV (Cayrel et al. 2004; Barbuy et al. 2011).

Stellar parameters for CS 31082-001 were adopted from Hill et al. (2002): $T_{\rm eff}$ = 4825 ± 50 K, log g = 1.5 ± 0.3, [Fe/H] = −2.9 ± 0.1 (in LTE), and $v_{\rm t}$ = 1.8 ± 0.2 km s^{-1}. We also adopted the light element abundances determined by Hill et al. (2002), Cayrel et al. (2004), and Spite et al. (2005).

The calculations used the Turbospectrum molecular line lists, described in detail by Alvarez & Plez (1998), together with the atomic line lists from the VALD2 compilation (Kupka et al. 1999). Some updated oscillator strengths are available in the literature: Cr I from Sobeck et al. (2007); Ge I from Biémont et al. (1999); La II from Lawler et al. (2001a); Ce II from Palmeri et al. (2000) and Lawler et al. (2009); Nd II from Den Hartog et al. (2003); Sm II from Lawler et al. (2006); Eu I and Eu II from Lawler et al. (2001b) and Den Hartog et al. (2002); Gd II from Den Hartog et al. (2006); Tb II from Lawler et al. (2001c); Dy II from Sneden et al. (2009); Er II from Lawler et al. (2008); Tm I and Tm II from Wickliffe & Lawler (1997) and Sneden et al. (2009); Lu I from Fedchak et al. (2000); Lu II from Quinet et al. (1999); Hf II from Lawler et al. (2007); Ta I from Fivet et al. (2006); W II from Nilsson et al. (2008).

Table 1. LTE abundances in CS 31082-001 as derived previously and in the present paper, and our adopted final abundances.

El.	Z	A(X) (1)	A(X) (2)	A(X) (3)	A(X) this work	A(X) adopted	[X/Fe] adopted
Ge	32	–	–	–	+0.10	+0.10 ± 0.21	–0.55
Sr	38	+0.72	–	–	–	+0.72 ± 0.10	0.73
Y	39	–0.23	–	–	–0.15	−0.19 ± 0.07	0.53
Zr	40	+0.43	–	–	+0.55	+0.49 ± 0.08	0.84
Nb	41	–0.55	–	–	–0.52	−0.54 ± 0.12	0.97
Mo	42	–	–	–	–0.11	−0.11 ± 0.13	0.90
Ru	44	+0.36	–	–	+0.36	+0.36 ± 0.12	1.45
Rh	45	–0.42	–	–	–0.42	−0.42 ± 0.12	1.39
Pd	46	–0.05	–	–	–0.09	−0.09 ± 0.07	1.18
Ag	47	–0.81	–	–	–0.84	−0.84 ± 0.21	1.15
Ba	56	+0.40	–	–	–	+0.40 ± 0.14	1.16
La	57	–0.60	–0.62	–	–	−0.62 ± 0.05	1.17
Ce	58	–0.31	–0.29	–	–0.31	−0.29 ± 0.05	1.03
Pr	59	–0.86	–0.79	–	–	−0.79 ± 0.05	1.38
Nd	60	–0.13	–0.15	–	–0.21	−0.15 ± 0.05	1.33
Sm	62	–0.51	–0.42	–	–0.42	−0.42 ± 0.05	1.51
Eu	63	–0.76	–0.72	–	–0.75	−0.72 ± 0.05	1.69
Gd	64	–0.27	–0.21	–	–0.29	−0.21 ± 0.05	1.61
Tb	65	–1.26	–1.01	–	–1.00	−1.01 ± 0.05	1.64
Dy	66	–0.21	–0.07	–	–0.12	−0.07 ± 0.05	1.73
Ho	67	–	–0.80	–	–	−0.80 ± 0.06	1.62
Er	68	–0.27	–0.30	–	–0.31	−0.30 ± 0.05	1.67
Tm	69	–1.24	–1.15	–	–1.18	−1.15 ± 0.05	1.64
Yb	70	–	–0.41	–	–	−0.41 ± 0.11	1.66
Lu	71	–	–	–	–1.08	−1.08 ± 0.13	1.73
Hf	72	–0.59	–0.72	–	–0.73	−0.72 ± 0.05	1.33
Ta	73	–	–	–	–1.60	−1.60 ± 0.23	1.47
W	74	–	–	–	–0.90	−0.90 ± 0.24	0.92
Re	75	–	–	–	–0.21	−0.21 ± 0.21	2.45
Os	76	+0.43	–	+0.18	–	+0.18 ± 0.07	1.72
Ir	77	+0.20	–	+0.20	–	+0.20 ± 0.07	1.72
Pt	78	–	–	+0.30	–	+0.30 ± 0.23	1.46
Au	79	–	–	-1.00	–	−1.00 ± 0.34	0.89
Pb	82	–	–	-0.65	–	−0.65 ± 0.19	0.25
Bi	83	–	–	-0.40	–	−0.40 ± 0.33	1.83
Th	90	–0.98	–	–	–	−0.98 ± 0.13	1.84
U	92	–1.92	–	–	–	−1.92 ± 0.17	1.68

References. (1) Hill et al. (2002); (2) Sneden et al. (2009); (3) Barbuy et al. (2011).

Following the same procedure as Barbuy et al. (2011), we computed synthetic spectra for all lines of the elements of interest from our line list, with different enhancement factors, in order to identify useful lines. All lines were checked for proper intensities and possible blends, and lines with major and/or uncertain blends were rejected. As discussed by Peterson et al. (2001), modeling the UV region is difficult because of the crowding of lines at short wavelengths. Another severe problem is the numerous "unknown" lines (i.e. line missing in the input line list), making it more difficult to normalize the UV continuum and match the observations and spectral synthesis calculations. Recently, Peterson (2011) has reported abundance determinations of molybdenum in five mildly to extremely metal-poor turnoff stars using near-UV spectra with a "guessed identifications" method of missing lines (for details on the procedure, see Peterson et al. 2001). Here, we preferred to reject lines seriously affected by these effects.

3.1. Final abundances

The selected lines and individual abundances are listed in Table A.1. Mean abundances A(X)[2] for 23 neutron-capture elements are given in Table 1 (Col. 6) and compared to previous results (Hill et al. 2002; Sneden et al. 2009). We have derived abundances for six new elements in CS 31082-001: germanium (Ge, Z = 32), molybdenum (Mo, Z = 42), lutetium (Lu, Z = 71), tantalum (Ta, Z = 73), tungsten (W, Z = 74), and rhenium (Re, Z = 75). The general agreement is discussed in Sect. 3.3. We also investigated the elements in the region between germanium and strontium, as well as elements between the first and second r-process peaks, but no useful line was found.

As noted above, many elements of the first and second r-process peaks in these metal-poor stars are observable from the ground, and several authors have presented analyses of them. So, for each element, we compared the new abundance with the previous data in order to adopt a final value. The results are shown in Cols. 7 and 8 of Table 1.

For comparison, Table 2 lists solar abundances from different authors (Anders & Grevesse 1989; Grevesse & Sauval 1998; Sneden et al. 2008; Asplund et al. 2009; Lodders et al. 2009; Caffau et al. 2011) for all elements of interest; the values from Lodders et al. (2009) and Caffau et al. (2011) are adopted here. We also present the solar system r- and s-process fractions from the deconvolution by Simmerer et al. (2004), and use them to compute the solar system r-process abundances.

3.2. Uncertainties on the derived abundances

As discussed by Cayrel et al. (2004), for a given stellar temperature, the ionization equilibrium provides an estimate of the stellar gravity with an internal accuracy of about 0.1 dex in $\log g$, and the microturbulence velocity v_t can be constrained within 0.2 km s^{-1}, making the temperature the largest source of uncertainty in the abundance determination. Cayrel et al. (2004) estimate that the total error in the adopted temperatures is of the order of 100 K, higher than the value found by Hill et al. (2002).

We estimate the abundance uncertainties arising from each of these three sources independently. The results are shown in Table 3 (Cols. 3 to 5), where the models B, C, and D are compared with our nominal model labeled A.

Since the stellar parameters are not independent of each other, the total error budget is not the quadratic sum of the various sources of uncertainties, but it does contain significant covariance terms. The solution was to create a new atmospheric model with a temperature higher by 100 K, thereby determining the corresponding surface gravity by requiring that the Fe derived from Fe I and Fe II lines be identical, and the microturbulent velocity by requiring that the abundance derived for each Fe I line be independent of the equivalent width of the line. Model E is the result of this exercise, with $T_{\rm eff}$ = 4925 K, $\log g$ = 1.8 dex, and v_t = 1.8 km s^{-1}; Table 3 (Col. 6) shows the abundance uncertainties arising from the stellar parameters.

Observational errors were estimated using the standard deviation of the abundances from individual lines for each element, taking the uncertainties in defining the continuum, fitting the line profiles, and in the oscillator strengths into account. For elements with only three useful lines, we conservatively adopted the observational error obtained for molybdenum as representative.

[2] We adopt the notation A(X) = $\log \epsilon$(X) = $\log n$(X)/n(H) + 12, with n = number density of atoms.

Table 2. Solar r- and s-process fractions (Simmerer et al. 2004) and total solar-system element abundances.

El.	Z	Fraction		$A(X)_\odot$				
		r	s	(1)	(2)	(3)	(4)	(5)
Fe	26	–	–	7.67	7.50	7.50	7.45	**7.52**
Ge	32	0.516	0.484	3.41	3.41	3.65	**3.58**	–
Sr	38	0.110	0.890	2.90	2.97	2.87	**2.92**	–
Y	39	0.281	0.719	2.24	2.24	2.21	**2.21**	–
Zr	40	0.191	0.809	2.60	2.60	2.58	**2.58**	–
Nb	41	0.324	0.676	1.42	1.42	1.46	**1.42**	–
Mo	42	0.323	0.677	1.92	1.92	1.88	**1.92**	–
Ru	44	0.610	0.390	1.84	1.84	1.75	**1.84**	–
Rh	45	0.839	0.161	1.12	1.12	0.91	**1.12**	–
Pd	46	0.555	0.445	1.69	1.69	1.57	**1.66**	–
Ag	47	0.788	0.212	1.24*	1.24*	0.94	**0.94**	–
Sn	50	0.225	0.775	2.0	2.0	2.04	**2.00**	–
Ba	56	0.147	0.853	2.13	2.13	2.18	**2.18**	–
La	57	0.246	0.754	1.22	1.17	1.10	**1.14**	–
Ce	58	0.186	0.814	1.55	1.58	1.58	**1.61**	–
Pr	59	0.508	0.492	0.71	0.71	0.72	**0.76**	–
Nd	60	0.421	0.579	1.50	1.50	1.42	**1.45**	–
Sm	62	0.669	0.331	1.00	1.01	0.96	**1.00**	–
Eu	63	0.973	0.027	0.51	0.51	0.52	0.52	**0.52**
Gd	64	0.819	0.181	1.12	1.12	1.07	**1.11**	–
Tb	65	0.933	0.067	0.33*	0.35*	0.30	**0.28**	–
Dy	66	0.879	0.121	1.10	1.14	1.10	**1.13**	–
Ho	67	0.936	0.064	0.26	0.26	0.48	**0.51**	–
Er	68	0.832	0.168	0.93	0.93	0.92	**0.96**	–
Tm	69	0.829	0.171	0.13*	0.15*	0.10	**0.14**	–
Yb	70	0.682	0.318	1.08	1.08	0.84	**0.86**	–
Lu	71	0.796	0.204	0.12*	0.06	0.10	**0.12**	–
Hf	72	0.510	0.490	0.88	0.88	0.85	0.88	**0.87**
Ta	73	0.588	0.412	0.13*	–0.13*	–0.12*	**–0.14***	–
W	74	0.462	0.538	0.68*	0.69*	0.85	**1.11**	–
Re	75	0.911	0.089	0.27*	0.28*	0.26*	**0.28***	–
Os	76	0.916	0.084	1.45	1.45	1.40	1.45	**1.36**
Ir	77	0.988	0.012	1.35	1.35	1.38	**1.38**	–
Pt	78	0.949	0.051	1.8	1.8	1.62*	**1.74**	–
Au	79	0.944	0.056	1.01	1.01	0.92	**1.01**	–
Pb	82	0.214	0.786	1.85	1.95	1.75	**2.00**	–
Bi	83	0.647	0.353	0.71*	0.71*	0.65*	**0.67***	–
Th	90	1.000	0.000	0.12	0.08*	0.02	<0.08	**0.08**
U	92	1.000	0.000	<–0.47	<–0.47	–0.54*	**<–0.47**	–

Notes. Adopted abundances are marked in boldface. (*) Meteoritic abundances.

References. (1) Anders & Grevesse (1989); (2) Grevesse & Sauval (1998); (3) Asplund et al. (2009); (4) Lodders et al. (2009); (5) Caffau et al. (2011).

For abundances based on only one or two lines we adopted an error of 0.2 dex (see Sect. 3.3.1).

Finally, we examined the resolution adopted for the synthetic spectrum calculation as another possible source of uncertainty. Barbuy et al. (2011) discuss this value (R = 30 800) in detail, including the effect of the instrumental profile, the macroturbulence and the rotational velocity of the star. Analyzing the lines again, we checked that a change of 8% in R induces a variation in the abundances of at most 0.05 dex, which we account for in the final error for all elements.

Table 3. Abundance uncertainties linked to stellar parameters.

A: $T_{\rm eff}$ = 4825, log g = 1.5 dex, $v_{\rm t}$ = 1.8 km s^{-1}				
B: $T_{\rm eff}$ = 4825, log g = 1.4 dex, $v_{\rm t}$ = 1.8 km s^{-1}				
C: $T_{\rm eff}$ = 4825, log g = 1.5 dex, $v_{\rm t}$ = 1.6 km s^{-1}				
D: $T_{\rm eff}$ = 4925, log g = 1.5 dex, $v_{\rm t}$ = 1.8 km s^{-1}				
E: $T_{\rm eff}$ = 4925, log g = 1.8 dex, $v_{\rm t}$ = 1.8 km s^{-1}				
El.	Δ_{B-A}	Δ_{C-A}	Δ_{D-A}	Δ_{E-A}
[Fe/H]	–0.01	+0.04	+0.06	+0.10
[Ge I/Fe]	+0.01	–0.03	+0.09	+0.05
[Y II/Fe]	–0.01	+0.12	+0.03	+0.05
[Zr II/Fe]	–0.01	+0.06	+0.02	+0.06
[Nb II/Fe]	–0.02	–0.02	+0.03	+0.09
[Mo II/Fe]	–0.02	–0.02	+0.01	+0.07
[Ru I/Fe]	+0.02	–0.03	+0.10	+0.04
[Rh I/Fe]	+0.02	–0.04	+0.09	+0.04
[Pd I/Fe]	+0.02	–0.02	+0.09	+0.04
[Ag I/Fe]	+0.02	–0.03	+0.10	+0.04
[Ce II/Fe]	–0.02	–0.03	+0.03	+0.08
[Nd II/Fe]	–0.02	–0.03	+0.03	+0.08
[Sm II/Fe]	–0.02	–0.02	+0.03	+0.08
[Eu II/Fe]	–0.01	+0.07	+0.03	+0.07
[Gd II/Fe]	–0.02	+0.01	+0.03	+0.07
[Tb II/Fe]	–0.02	–0.02	+0.03	+0.08
[Dy II/Fe]	–0.01	+0.07	+0.03	+0.06
[Er II/Fe]	–0.02	+0.01	+0.02	+0.07
[Tm II/Fe]	–0.02	–0.01	+0.02	+0.07
[Lu II/Fe]	–0.02	–0.03	+0.01	+0.07
[Hf II/Fe]	–0.02	–0.01	+0.03	+0.08
[Ta II/Fe]	–0.03	–0.03	+0.04	+0.11
[W II/Fe]	–0.03	–0.02	+0.05	+0.12
[Re II/Fe]	–0.03	–0.02	–0.01	+0.06

3.3. Elements of the first peak

3.3.1. Germanium (Z = 32)

The Ge I 3039.067 Å line is the main abundance indicator for this element. Using the Biémont et al. (1999) gf-value we determined an abundance of A(Ge) = 0.10 ± 0.21 dex, the first detection of this element in CS 31082-001. Since we only used one line, we carefully checked the influence of the placement of the continuum on the derived abundance, as shown in Fig. 1, and derived an observational error of σ = 0.2 dex as a good value for this and other elements which exhibit only one or two lines. In fact, since such lines typically have a better continuum definition than the Ge line, we consider 0.2 dex to be an upper limit, in particular with the new higher resolution UVES spectrum.

Our result of [Ge/Fe] = −0.55 agrees with those found by Cowan et al. (2002, 2005) in metal-poor Galactic-halo stars, showing that germanium is strongly depleted compared to the solar abundance, even in r-element-rich metal-poor stars.

3.3.2. Yttrium (Z = 39)

Using 13 new Y II lines, in addition to the two lines used by Hill et al. (2002), we determined an abundance of A(Y) = −0.15 ± 0.07 dex for this element, in agreement with A(Y) = −0.23 ± 0.12 dex found previously. The lines in common between Hill et al. (2002) and the present work give consistent results, and we adopt the average A(Y) = −0.19 ± 0.07 dex ([Y/Fe] = 0.53) as the final abundance.

Recently, Hansen et al. (2012) analyzed a sample of metal-poor stars, including CS 31082-001. They also adopted MARCS models, but a slightly different set of atmospheric parameters for CS 31082-001 ($T_{\rm eff}$ = 4925 K, log g = 1.51 [cgs], $v_{\rm t}$ = 1.4, [Fe/H] = −2.81). For the spectrum synthesis they adopted

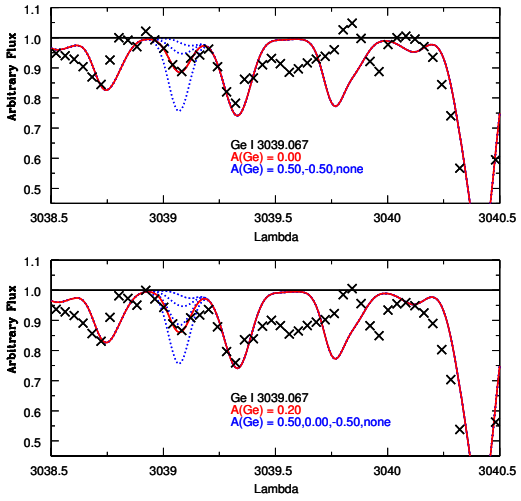

Fig. 1. Fits of the Ge I 3039.067 Å line in CS 31082-001 for two different placements of the continuum. Crosses: observations. Dotted lines: synthetic spectra computed for the abundances indicated in the figure. Solid line: synthetic spectrum computed with the best abundance, also indicated in the figure.

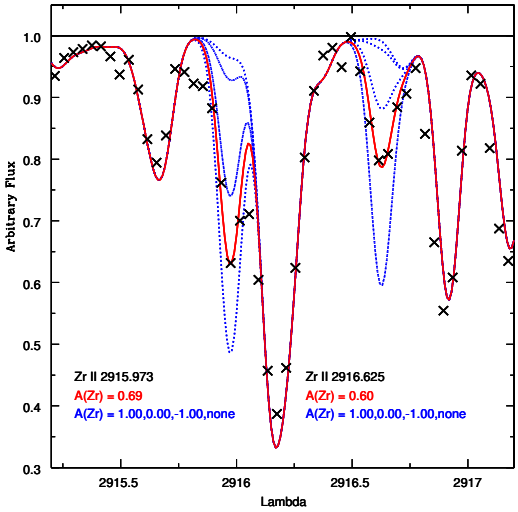

Fig. 2. Fits of the Zr II 2915.973 Å and Zr II 2916.625 Å lines in CS 31082-001. Symbols as in Fig. 1.

MOOG (Sneden 1973, version 2009 including treatment of scattering). The differences between their [X/Fe] results and ours are in general below 0.1 dex, but for yttrium they find [Y/Fe] = 0.82, 0.29 dex higher than our adopted value.

We decided to check this comparison in a homogeneous way, using the Turbospectrum code and the lines from Hansen et al. (2012) with our set of atmospheric parameters to determine the Y abundance in CS 31082-001, as well as with their values.

We find [Y/Fe] = 0.47 with our original atmospheric parameters, while the atmospheric parameters of Hansen et al. (2012) give the relative abundance [Y/Fe] = 0.71; the difference of 0.24 is very close to the previous one. However, we found a stronger correlation between the individual abundances and the equivalent widths with the atmospheric parameters adopted by Hansen et al. (2012), suggesting that their microturbulent velocity may be underestimated. In fact, when only changing the v_t in their set of atmospheric parameters to our microturbulent velocity we found [Y/Fe] = 0.47, in agreement with our adopted value, confirming the problem with their v_t. Yttrium is particularly sensitive to this effect because several Y lines are relatively strong.

3.3.3. Zirconium (Z = 40)

More than 25 Zr II profiles were checked in the STIS spectrum, but we decided to keep only the 12 best lines. Together with 46 new useful UVES lines, we find a final abundance A(Zr) = +0.55 ± 0.08 dex for zirconium, in agreement with the value A(Zr) = +0.43 ± 0.14 dex from Hill et al. (2002). Figure 2 shows two fits of lines used in this work. The Zr II line 2758.792 Å gives an abundance of A(Zr) = −0.07 dex, despite a good fit, suggesting there is a problem with the gf-value of the transition; thus, we exclude this line from the average. The same applies to Zr II 3556.585 Å, which gives A(Zr) = 0.00 dex. We are using a larger set of lines than in previous work, and the abundances by Hill et al. (2002) can be considered as a subset of our data. Finally, the line Zr II 3030.915 Å was used with both STIS and UVES spectra, with consistent results. In summary, the average A(Zr) = +0.49 ± 0.08 dex ([Zr/Fe] = 0.84) is our best value for the final abundance.

3.3.4. Niobium (Z = 41)

Only one line was used by Hill et al. (2002) to derive A(Nb) = −0.55 ± 0.20 dex. We found nine useful Nb II lines in our STIS spectra, from an initial set of more than 70 lines, giving an average abundance of A(Nb) = −0.52 ± 0.11 dex, in good agreement with the previous value. In Fig. 3 we show an example of fit to a Nb II line.

It was again possible to use the same line Nb II 3028.433 Å in both sets of spectra, and the results agree well, providing an average value for our adopted niobium abundance, A(Nb) = −0.54 ± 0.12 dex ([Nb/Fe] = 0.97).

3.3.5. Molybdenum (Z = 42)

After checking almost 50 Mo lines, only three Mo II useful lines were retained, giving A(Mo) = −0.11 ± 0.13 dex ([Mo/Fe] = 0.90) – the first published value for A(Mo) in this star. The lines 2660.576 Å and 2871.507 Å are shown in Figs. 4 and 5.

3.3.6. Ruthenium (Z = 44)

The VALD atomic data for many Ru I lines give equivalent widths that are too strong, as discussed by Barbuy et al. (2011), and new laboratory oscillator strengths have not been found in the recent literature. We tried to use one Ru I line to determine a new UV abundance from STIS and found A(Ru) = +0.65 dex, higher than the previous result A(Ru) = +0.36 ± 0.17 dex from Hill et al. (2002), confirming the impossibility of using this region of the STIS spectra for this element.

We calculated the abundance again using the three lines observed in our new UVES spectrum, and also used by Hill et al. (2002), and found A(Ru) = 0.36 ± 0.12 dex ([Ru/Fe] = 1.45), in very good agreement with the previous work.

3.3.7. Rhodium (Z = 45)

Using three good Rh I lines, we determined A(Rh) = −0.42 ± 0.12 dex ([Rh/Fe] = 1.39) for this element. Our new result is in complete agreement with A(Rh) = −0.42 ± 0.16 dex from Hill et al. (2002), and was adopted as the final abundance.

3.3.8. Palladium (Z = 46)

Adding the line Pd I 3516.944 Å to the original line set from Hill et al. (2002), our earlier and new UVES spectra give A(Pd) =−0.09 ± 0.07 dex, in good agreement with A(Pd) = −0.05 ± 0.18 dex from the previous work. We adopted our new result, [Pd/Fe] = 1.18 as the final abundance.

3.3.9. Silver (Z = 47)

For this element, only the same Ag I lines 3280.679 Å and 3382.889 Å, as used by Hill et al. (2002), were useful in the new UVES spectrum. Our new analysis gives A(Ag) = −0.84 ± 0.21 dex ([Ag/Fe] = 1.15) as the final abundance, in agreement with the previous result A(Ag) = −0.81 ± 0.24 dex. The lower error found in the present work is probably due to the better quality of the new UVES spectrum in the near-UV region.

3.4. Elements of the second peak

3.4.1. Barium (Z = 56)

This is another element studied by Hansen et al. (2012) in CS 31082-001 with a big difference when compared with previous results. They found [Ba/Fe] = 1.43, which is 0.27 dex higher than the value from Hill et al. (2002). While that abundance was derived from six Ba II lines, Hansen et al. (2012) used only two of them, Ba II 4554.03 Å and Ba II 5853.67 Å, leading us to check these results again.

In addition to the comments made in the case of yttrium, we also adopted the same reference for the hyperfine structure of barium (McWilliam 1998). The final abundance was calculated with the weighting method suggested by the authors to provide a genuine comparison (for details, see Hansen et al. 2012). We found [Ba/Fe] = 1.04 with our original atmospheric parameters, while the set from Hansen et al. (2012) gave the relative abundance [Ba/Fe] = 1.30. The difference between the results is 0.26, very close to the previous difference. Since the barium lines are strong, we explain this difference as effect of the microturbulence velocity, and we decided to keep the result from Hill et al. (2002) as the final abundance. Considerations about the non-LTE (NLTE) corrections on this result can be found in Sect. 3.5.

3.4.2. Cerium (Z = 58)

By using ten new lines of Ce II, we were able to determine the abundance A(Ce)= −0.31 ± 0.10 dex, in very good agreement with the value from Hill et al. (2002). However, Sneden et al. (2009) determined a more precise abundance using 38 lines for this element, leading us to adopt their result A(Ce) = −0.29 ± 0.05 dex ([Ce/Fe] = 1.03) as the final abundance.

3.4.3. Neodymium (Z = 60)

We derived A(Nd)= −0.21 ± 0.10 dex from the 18 useful Nd II lines in the region covered by the new UVES spectrum, in agreement with A(Nd) = −0.13 ± 0.13 dex found by Hill et al. (2002) and with A(Nd) = −0.15 ± 0.05 dex by Sneden et al. (2009), despite the lower absolute value. In fact, even using only the subset of lines with improved atomic data, we found A(Nd) = −0.24 ± 0.10 dex, quite similar to the complete set. Other authors use sets of lines covering the entire optical region, and we adopted the result from Sneden et al. (2009) [Nd/Fe] = 1.33 as the final abundance, since they have used the most complete line list for this element.

3.4.4. Samarium (Z = 62)

This element presents 23 useful lines in the region studied, and we found A(Sm) = −0.42 ± 0.09 dex from our data set, in complete agreement with A(Sm) = −0.42±0.05 dex ([Sm/Fe] = 1.51) from Sneden et al. (2009). We decided to adopt that abundance, since the number of lines used is considerably higher, making the error smaller and the result more reliable.

3.4.5. Europium (Z = 63)

After checking more than 20 line profiles, we derived A(Eu) = −0.75 ± 0.22 dex from the best Eu II line 2906.669 Å, in agreement with A(Eu) = −0.72 ± 0.05 dex from Sneden et al. (2009). Figure 6 shows our fit to this line. We adopted the value from Sneden et al. (2009) as more reliable, ([Eu/Fe] = 1.69) given the higher number of lines used.

3.4.6. Gadolinium (Z = 64)

This element shows several lines in this region, and we derived its abundance using 32 Gd II lines. We found A(Gd) = −0.29 ± 0.09 dex, in agreement with A(Gd) = −0.21 ± 0.05 from Sneden et al. (2009).

In this work we are using the same references as Sneden et al. (2009) for new atomic data, but not all the transitions have been updated by Den Hartog et al. (2006), so we adopted the value from Sneden et al. (2009) as more reliable ([Gd/Fe] = 1.61).

3.4.7. Terbium (Z = 65)

This is the most problematic element as regards consistency with previous abundance results. Hill et al. (2002) found A(Tb) = −1.26 ± 0.12 dex with σ = 0.07 from seven optical lines using the UVES spectra, while Sneden et al. (2009) found A(Tb) = −1.01 ± 0.05 dex with σ = 0.04 from nine lines using updated oscillator strengths from Lawler et al. (2001c). Here, we could use three Tb II lines to derive A(Tb) = −1.00 ± 0.14 dex. For the line 2934.802 Å no new gf-value is available, so it was excluded from the average despite a good fit.

Our new result confirms the higher abundance found by Sneden et al. (2009) from a larger set of lines, and we adopted [Tb/Fe] = 1.64 as the more reliable result.

3.4.8. Dysprosium (Z = 66)

From 26 lines in the region studied, we found A(Dy) = −0.16 ± 0.09 dex. By selecting only lines with new atomic data, we found A(Dy)= −0.12 ± 0.09 dex, in agreement with A(Dy) = −0.07 ± 0.05 dex from Sneden et al. (2009). We adopted [Dy/Fe] = 1.73 from Sneden et al. (2009) as the final abundance.

3.4.9. Erbium (Z = 68)

After checking several Er lines, we derived A(Er) = −0.31 ± 0.09 dex from 17 good lines of Er II. Figure 7 shows a sample fit to an Er II line. Our result agrees with A(Er) = −0.27 ± 0.15 dex found by Hill et al. (2002) and A(Er) = −0.30 ± 0.05 dex by Sneden et al. (2009), who used the same source of atomic data.

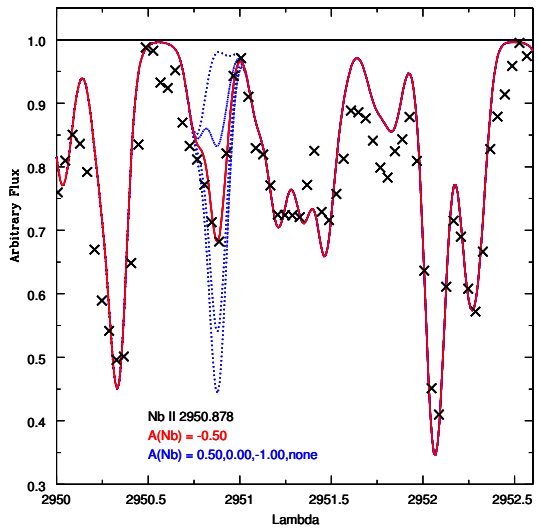

Fig. 3. Fit of the Nb II 2950.878 Å line in CS 31082-001. Symbols as in Fig. 1.

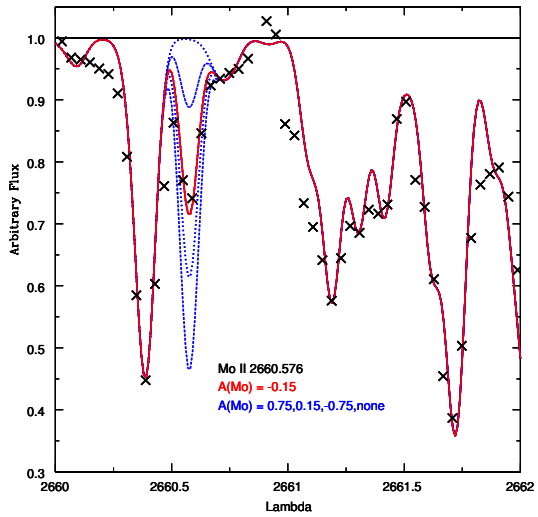

Fig. 4. Fit of the Mo II 2660.576 Å line in CS 31082-001. Symbols as in Fig. 1.

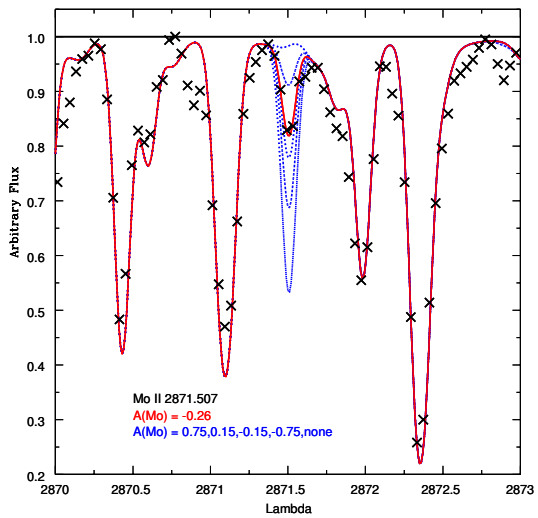

Fig. 5. Fit of the Mo II 2871.507 Å line in CS 31082-001. Symbols as in Fig. 1.

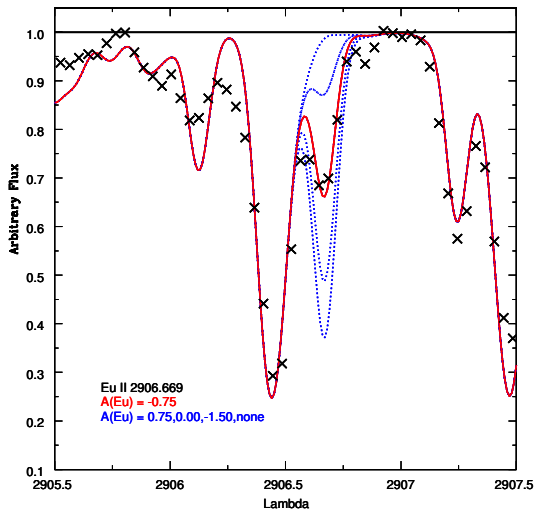

Fig. 6. Fit of the Eu II 2906.669 Å line in CS 31082-001. Symbols as in Fig. 1.

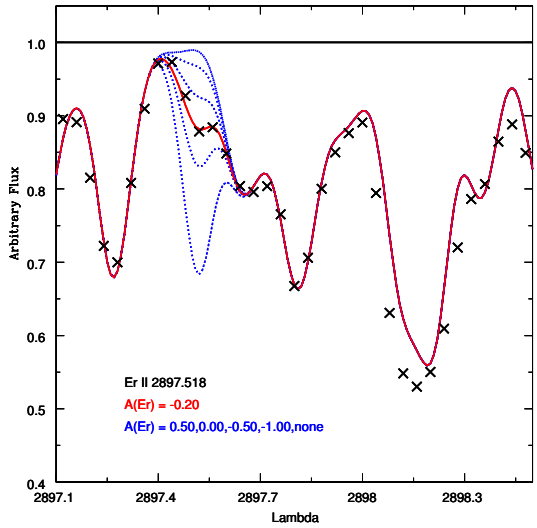

Fig. 7. Fit of the Er II 2897.518 Å line in CS 31082-001. Symbols as in Fig. 1.

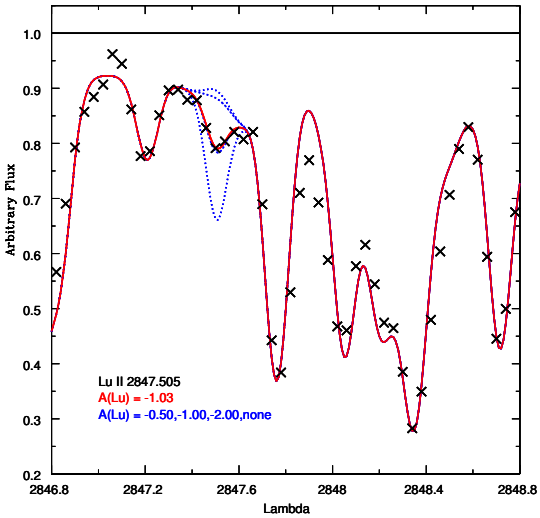

Fig. 8. Fit of the Lu II 2847.505 Å line in CS 31082-001. Symbols as in Fig. 1.

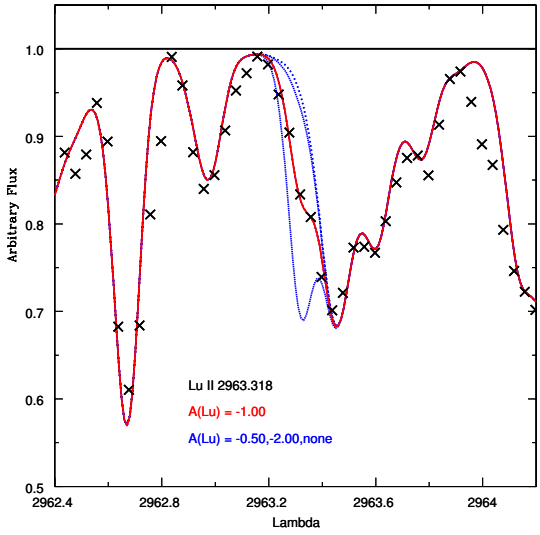

Fig. 9. Fit of the Lu II 2963.318 Å line in CS 31082-001. Symbols as in Fig. 1.

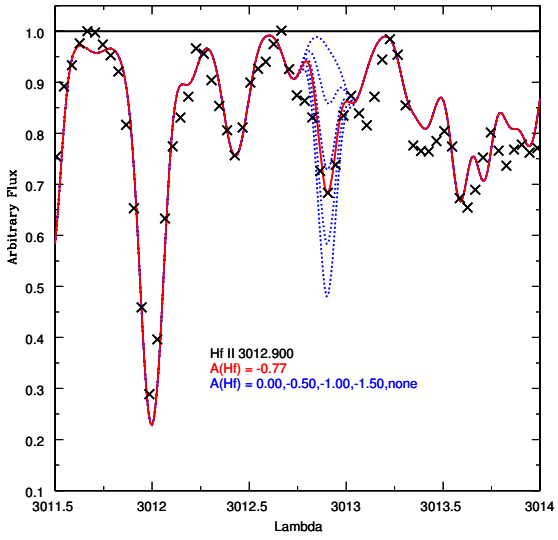

Fig. 10. Fit of the observed Hf II 3012.900 Å line in CS 31082-001. Symbols as in Fig. 1.

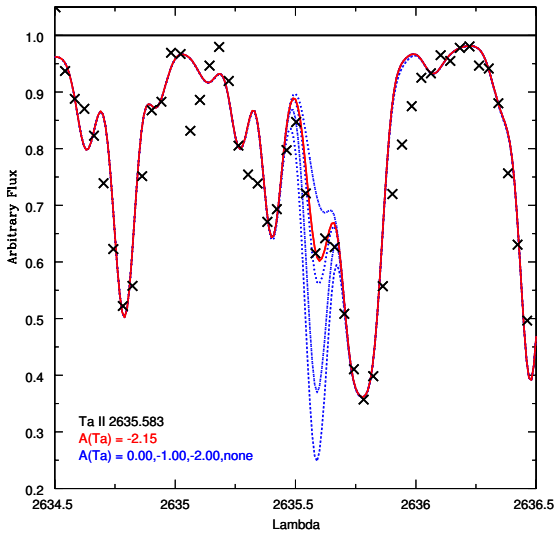

Fig. 11. Fit of the Ta II 2635.583 Å line in CS 31082-001. Symbols as in Fig. 1.

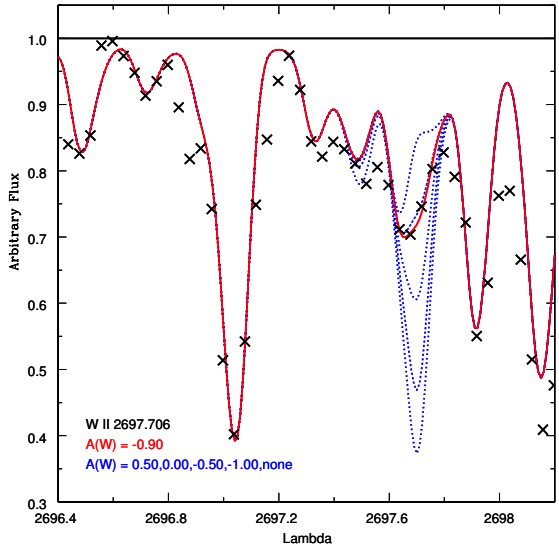

Fig. 12. Fit of the W II 2697.706 Å line in CS 31082-001. Symbols as in Fig. 1.

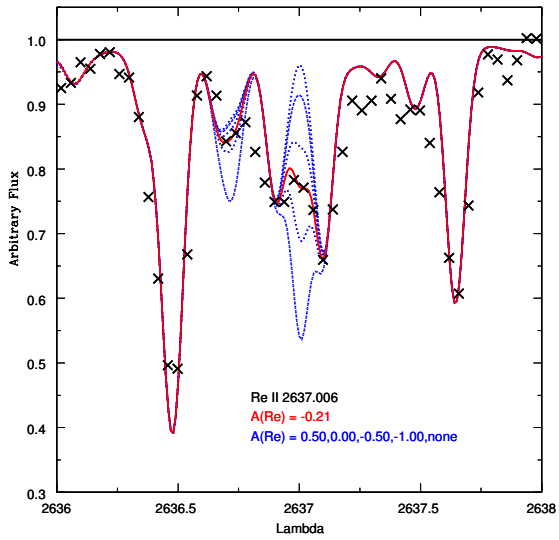

Fig. 13. Fit of the Re II 2637.006 Å line in CS 31082-001. Symbols as in Fig. 1.

However, as Sneden et al. (2009) derived their result from 19 erbium lines, we adopt their value, [Er/Fe] = 1.67, as the most reliable.

3.4.10. Thulium (Z = 69)

From several Tm lines, we used the best nine to derive A(Tm) = −1.18±0.10 dex, in agreement with A(Tm) = −1.24±0.13 dex by Hill et al. (2002) and A(Tm) = −1.15 ± 0.05 dex by Sneden et al. (2009).

3.4.11. Lutetium (Z = 71)

Another element newly measured in CS 31082-001. The adopted abundance is A(Lu) = −1.08 ± 0.13 dex ([Lu/Fe] = 1.73), as the mean of the three best Lu II lines in our data (see Figs. 8 and 9).

3.4.12. Hafnium (Z = 72)

After checking more than 60 Hf lines, we derived A(Hf) = −0.73 ± 0.11 dex from five lines that were not affected by unidentified lines or other problems. Figure 10 shows a sample fit to a Hf II line. Our result is in good agreement with A(Hf) = −0.72±0.05 dex ([Hf/Fe] = 1.33) from Sneden et al. (2009), who used new atomic data from Lawler et al. (2007); and we adopt this result.

3.4.13. Tantalum (Z = 73)

Ta has also not been analyzed before in CS 31082-001. As discussed in Barbuy et al. (2011), this is another element that presents many lines that are too strong in the synthetic spectra. We found new oscillator strengths for five Ta I lines in Fivet et al. (2006), but they were all rejected due to the crowding problems typical of the UV region. We therefore tried to use three other Ta II lines present in the spectrum.

Ta II 2685.190 Å gives A(Ta) = −2.80 dex, but the synthetic line is quite strong, and its oscillator strength is probably not correct. On the other hand, Ta II 2832.702 Å gives an abundance of A(Ta) = −1.05 dex with a good fit, although the line is weak. Another abundance indicator is the Ta II 2635.583 Å line, shown in Fig. 11, which yields A(Ta) = −2.15 dex. The final tantalum abundance is the average of the last two lines, A(Ta) = −1.60 ± 0.23 dex ([Ta/Fe] = 1.47).

3.4.14. Tungsten (Z = 74)

From our set of W II lines, most have new atomic data by Nilsson et al. (2008). We derived A(W) = −0.90 ± 0.24 dex ([W/Fe] = 0.92) using our best line W II 2697.706 Å, shown in Fig. 12, another first determination in this star.

3.4.15. Rhenium (Z = 75)

Re is the heaviest element analyzed in this work and also a first for this star. We derive A(Re) = −0.21±0.21 dex ([Re/Fe] = 2.45) from our two best lines Re I 2930.613 Å and Re II 2637.006 Å (see Fig. 13). Together with tungsten, rhenium is extremely important for studying the transition region between the second and third peaks of the r-process.

3.5. NLTE and 3D corrections

Andrievsky et al. (2009, 2011) reanalyzed the sample of EMP stars previously studied in the "First Stars" program, including CS 31082-001, determining in particular the abundance of Sr and Ba from NLTE computations. For Sr, the NLTE abundance is 0.2 dex lower than the LTE value found in Hill et al. (2002) ($[\mathrm{Sr/Fe}]_{\mathrm{NLTE}}$ = 0.53), while a larger correction to the Ba abundance was found; the NLTE value is A(Ba) = 0.00 dex ($[\mathrm{Ba/Fe}]_{\mathrm{NLTE}}$ = 0.76).

Recently, Mashonkina et al. (2012) have considered the ultraviolet overionization to calculate the NLTE abundance of Pb in cool stars from the Pb I line 4057 Å. In the case of CS 31082-001, the corrected value is A(Pb) = +0.01 ($[\mathrm{Pb/Fe}]_{\mathrm{NLTE}}$ = 0.94), substantially higher than the previous LTE abundances A(Pb) = −0.55 from Plez et al. (2004) and A(Pb) = −0.65 from Barbuy et al. (2011). For completeness, we also present the NLTE abundance for europium calculated by Mashonkina et al. (2012), 0.06 dex higher ($[\mathrm{Eu/Fe}]_{\mathrm{NLTE}}$ = 1.75) than the best LTE value A(Eu) = −0.72 dex from Sneden et al. (2009).

For the other heavy elements NLTE corrections are not available. It would be particularly interesting to check the NLTE effects on the Ge abundances, since the main abundance indicator for this element is a transition from the non-ionized state.

It is well known that NLTE calculations relative to LTE have effects on the abundances that are counterbalanced by taking 3D modeling into account; therefore both effects should be computed at the same time. In fact, since the lead abundance is an important calibration point for zero-age r-process abundance distribution models (Schatz et al. 2002; Wanajo 2007), and the NLTE correction found in the literature is sufficiently high to have implications for the discussion of r-process models for the heaviest neutron-capture elements in this star, we calculated the 3D correction for the abundance of this element.

To estimate the 3D correction we used a hydrodynamical model computed with the code CO5BOLD (Freytag et al. 2002, 2012) with parameters 5020/2.5/−3/0. The model has a resolution of 160×160×200, and its dimension is 573 215×573 214×245 362 km^3. Twenty representative snapshots have been selected, covering 156 h in time. For the opacity, based on the MARCS stellar atmosphere package (Gustafsson et al. 2008), the absorption coeffcients were averaged in six bins. The plane parallel $1\mathrm{D}_{\mathrm{LHD}}$ model was used as reference model, computed with the LHD code that shares the micro-physics and opacity with the CO5BOLD code.

The 3D correction is defined as $A(3\mathrm{D})$-$A(1\mathrm{D}_{\mathrm{LHD}})$ (for details, see Caffau et al. 2011). The line formation computations were done with Linfor3D[3]. Compared with the 1D LTE value, the 3D effect leads to a correction of ΔA(Pb) = −0.21 dex, which, together with the NLTE correction, gives a new lead abundance of A(Pb) = −0.20 dex ($[\mathrm{Pb/Fe}]_{\mathrm{NLTE}}$ = 0.73). As discussed by Spite et al. (2012), weaker lines form in deeper layers, where the granulation velocities and intensity contrast are higher, which is a possible explanation for this significant correction to the lead abundance.

It is important to note that our correction is not a full 3D NLTE computation, which has only been performed for Li I and O I so far. But while these complete models seem to be important in the Li case (Asplund et al. 2003; Barklem et al. 2003; Cayrel et al. 2007; Sbordone et al. 2010), the NLTE corrections for O I are quite similar in the 3D and 1D cases, at least with the solar parameters (Asplund et al. 2004).

4. Discussion

4.1. Comparison with the solar system r-process pattern

The abundances in CS 31082-001 from previous papers (Hill et al. 2002; Sneden et al. 2009) and from the present analysis are compared with each other in Table 1. A comparison of the observed abundance pattern with scaled solar system r-process abundances, using the deconvolution by Simmerer et al. (2004), is shown in Fig. 14, together with the residuals. The figure includes the results from Barbuy et al. (2011) for the third-peak r-process elements. For the radioactive elements U and Th, we show the abundance corrected for radioactive decay since the formation of the solar system, and those observed today. In addition, NLTE abundances for some elements (red dots and corresponding error bars), when available, are compared with the

[3] http://www.aip.de/~mst/Linfor3D/linfor_3D_manual.pdf

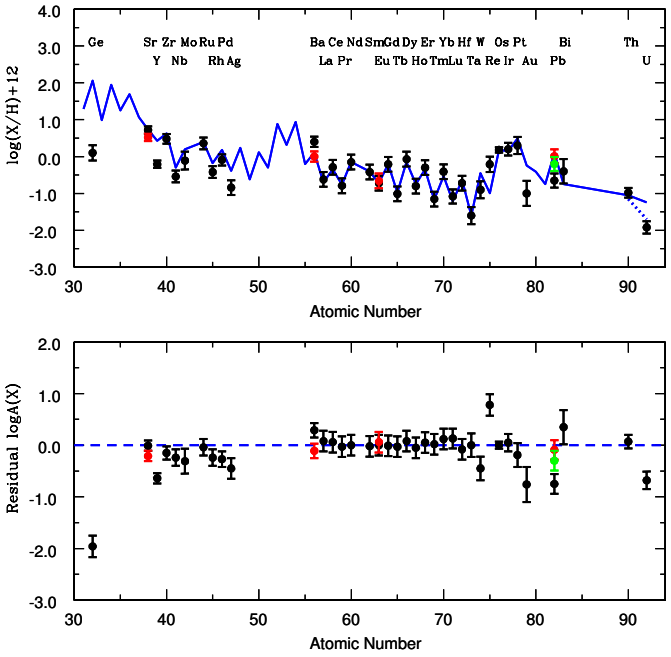

Fig. 14. Solar r-process abundance values. *Top*: deconvolution from Simmerer et al. (2004) scaled to Eu (solid line) compared with the new observed abundances in CS 31082-001 (black dots and respective error bars). Radioactive element (Th and U) abundances are corrected for radioactive decay since the formation of the solar system. The dotted line shows the abundances observed today for these two species. *Bottom*: abundance residuals. NLTE abundances for some elements (red dots and respective error bars) are compared with the LTE results. For Pb, the green symbol represents the NLTE+3D corrected value.

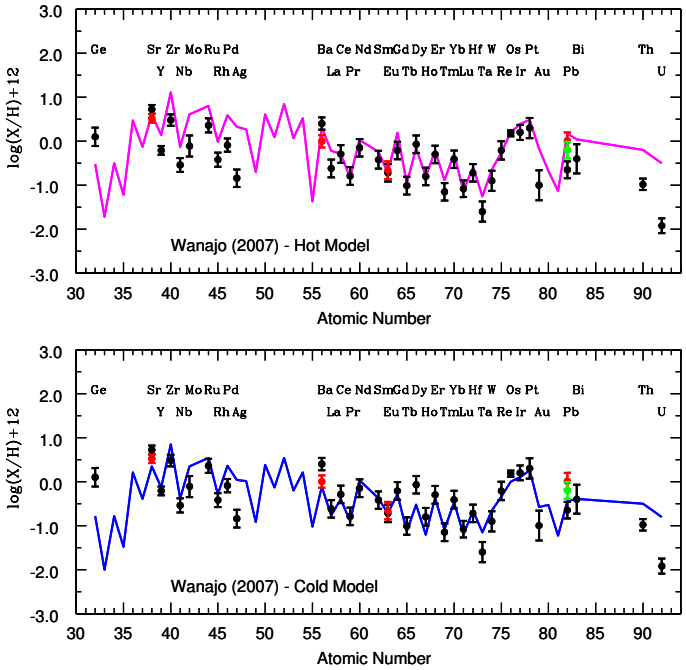

Fig. 15. Predicted abundance patterns for the hot (*upper*) and cold (*lower*) models by Wanajo (2007) (solid lines), compared with the new observed abundances in CS 31082-001. Symbols as in Fig. 15.

LTE results, and for lead we also present the new NLTE+3D corrected abundance (green symbol).

Figure 14 shows the NLTE corrected abundances compared with the LTE result and with the solar system r-process abundances. It is seen that the NLTE corrections from Andrievsky et al. (2011) make the Sr abundance more similar to the trends of the other elements from the first peak, and that the NLTE Ba abundance from Andrievsky et al. (2009) is in good agreement with the solar system r-process pattern. Finally, Fig. 14 shows that the new NLTE+3D lead abundance is in better agreement with, but still lower than, the solar system r-process value.

As discussed in some detail in the last section, there is good consistency between the different observational results for each element. Furthermore, Fig. 14 shows that the neutron-capture element distribution in the star matches a scaled solar r-process pattern very well, from Ba (Z = 56) through the third r-process peak. This well-known result in the context of metal-poor stars enriched in r-process elements had led some authors to argue that this extremely close agreement is evidence of the robust nature of the r-process, operating in much the same manner over the lifetime of the Galaxy. Our new abundances for lutetium and tantalum follow this trend, but while the tungsten value seems to be sub-solar, rhenium is overabundant. The disagreement can originate in a breakdown of the universality for Z = 74–75, from our spectrum and/or the atomic data, but another possible error source is the solar system r-process deconvolution (Goriely 1999).

Sneden et al. (2008) present an abundance comparison in their Fig. 11 with extensive elemental data for six r-process-rich stars, including CS 31082-001, showing exactly the consistency between the abundances of the heavier stable neutron-capture elements and the solar system r-process abundance distribution. This group of stars has been identified as standard templates to characterize the r-process nucleosynthesis pattern. At the same time, the comparison shows that the match between the stellar r-process abundances and the scaled solar system r-process pattern does not extend to the lighter heavy elements, and Fig. 14 illustrates this well-known result for the specific case of CS 31082-001 with the new abundance determinations for molybdenum and germanium.

Recently, Roederer et al. (2010a) and Cowan et al. (2011) have proposed that, similarly to the need for having several mechanisms operating in order to explain the origin of the lightest trans-Fe elements, a simple linear combination of the scaled solar system s-process and r-process is an inadequate description of some of the heavy neutron-capture elements, when a precise deconvolution is desired. On the other hand, the standard method of computing r-process residuals by solar deconvolution is still adequate for assessing the relative dominance of the s- or r-process in a general sense.

In addition, as discussed in Barbuy et al. (2011), we also see discrepancies between observation and theory among the heaviest elements from the third r-process peak and the actinides; notably, the high ages derived from the U/Os, U/Ir, and U/Pt ratios in radioactive chronometry would indicate that the nuclear data and/or astrophysical modeling of the element production need improvement. On the other hand, the fact that a strong actinide boost is observed in CS 31082-001, but not in other r-II stars like HE 1523-0901, suggests that the production of the heaviest elements in the r-process site(s) is more complex than assumed so far.

4.2. Comparison with r-process models

Figure 15 compares the predictions of the hot and cold models by Wanajo (2007) with the observed abundances in CS 31082-001, including the new elements derived in this paper,

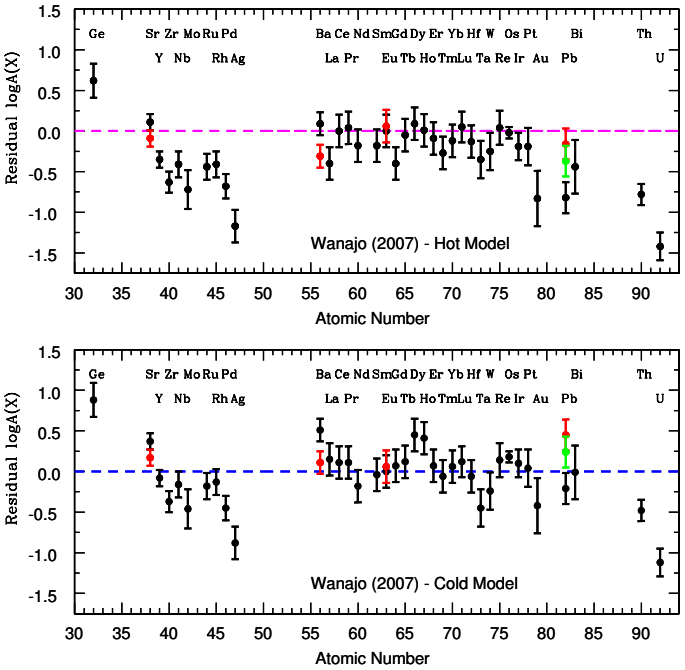

Fig. 16. Abundance residuals of elements in CS 31082-001 from the two Wanajo (2007) model predictions. Symbols as in Fig. 15.

while Fig. 16 shows the corresponding residuals. The abundances obtained from these nucleosynthesis calculations are based on supernova neutrino wind models with updated nuclear input data (based on the HFB-9 model of Goriely et al. 2005). These data update the older calculations by Wanajo et al. (2002), who adopted a cold r-process that proceeds with competing (n, γ) and β-decays, but without (γ, n) decays, when the temperature drops down to 1.0×10^8 K. This differs from the traditional (hot) r-process at a temperature of 1.0×10^9 K, where the (n, γ)–(γ, n) equilibrium remains a good approximation during r-processing.

The hot model fits many of the second-peak elements well, but fails for the first-peak elements and the heaviest third-peak elements. The cold model gives an overall better fit, except for Ba, Dy, Ho, and Os. This might suggest that the abundance pattern results from nucleosynthetic processes in several different physical conditions. It is also worth noting that both the hot and cold models fit our new Lu, W, and Re abundances very well (two of which show poor agreement with the solar r-pattern in Fig. 14), despite the failure to fit the Ta abundance. We note that it is the first time that abundances of elements from the region between the second and third peaks are given for an EMP star.

An important difference between the models is the behavior of the abundance pattern for the heaviest elements of the third peak. While the traditional "hot model" from Wanajo et al. (2002) produces abundances of gold, lead, and bismuth that are substantially higher than the observed values, the cold model seems to give a better description of this region, as discussed in Barbuy et al. (2011). Albeit more subtly, the new NLTE+3D Pb abundance leads us to the same conclusion. It would be interesting to check these corrections with the other elements in this region, but NLTE corrections for gold and bismuth are not available in the literature, nor are 3D corrections.

Recently, Farouqi et al. (2010) have investigated the termination point of charged-particle freezeout. They define a maximum entropy for a given expansion velocity and electron abundance (Y_e), beyond which the seed production of heavy elements fails, owing to the very low matter density. They also investigated an r-process subsequent to the charged-particle freeze-out, analyzing the impact of nuclear properties from different theoretical mass models on the final abundances. They find that it is possible to co-produce the light p-, s-, and r-process isotopes between Zn ($Z = 30$) and Ru ($Z = 44$) at Y_e in the range 0.450–0.498 and low entropies of $S < 100$–$150\ k_B$ (Boltzmann constant) per nucleon (see also similar discussion in Hoffman et al. 1996; Wanajo 2006). They also show that for Y_e slightly below 0.50, only the mass region below the mass number $A = 130$ peak can be formed, and the classical "main" r-process region up to the full third peak requires somewhat more neutron-rich winds.

Figure 17 shows the results from Farouqi et al. (2010) with $Y_e = 0.498$ and $Y_e = 0.482$, compared with the observed abundances in CS 31082-001. The calculations were performed with a selected constant expansion velocity of $V_{exp} = 7500$ km s^{-1}, and for each Y_e the superposition of the entropies spans from $S = 5\ k_B$/nucleon to the maximum entropy $S_{final}(Y_e) \sim 300\ k_B$/nucleon. One can see that the entire mass region from Sr up to Th can be fitted by using different parameters, in agreement with the need for more than one site for the r-process and/or different conditions in the same environment. This study can be seen as a generalization of the hot and cold models from Wanajo (2007), since the parameterization should reach the entire range of possibilities.

4.3. Origin of germanium

Another important approach to understanding the origin of the elements is to check the evolution of their abundances as a function of metallicity, from a sample of stars. However, for some elements, the number of stars with known abundances is still small due to the difficulty of detection; this is the case for germanium and molybdenum. Cowan et al. (2005) used a sample of ten metal-poor Galactic halo stars with measures of Ge to analyze the behaviour of this light element compared to the principal r-process patterns, represented by the Eu abundance. The sample includes the r-poor star HD 122563.

We reproduce the original comparison, including CS 31082-001 in the sample with our new Ge abundance. The result is shown in Fig. 18. One sees that CS 31082-001 is the most metal-poor star in the sample (Fig. 18, top), with the largest enrichment with r-process elements (Fig. 18, bottom). The Ge abundance is correlated with metallicity, but seems to be uncorrelated with the r-process elements. The authors also discuss that while neutron-capture processes are important for Ge production in solar system material, these abundance comparisons immediately suggest a different origin for this element early in the history of the Galaxy.

It is important to note that the neutrino-driven wind always predicts Ge/Sr < 1, because the high entropy ($S > 30\ k_B$/nucleon) leads to charged-particle freezeout from nuclear statistical equilibrium (NSE) and places the abundance peak at the $N = 50$ nuclei ^{88}Sr, ^{89}Y, and ^{90}Zr (Woosley & Hoffman 1992; Meyer et al. 1998; Wanajo & Ishimaru 2006). In contrast, the early convective ejecta from O-Ne-Mg (electron-capture) supernovae predict Ge/Sr ~ 1, because the low entropy ($S \sim 10\ k_B$/nucleon) with mild neutron-richness (Y_e down to 0.4) leads to an abundance peak at $A = 70$–80 ($N < 50$), including Ge, in NSE (Hartmann et al. 1985; Wanajo et al. 2011).

In Fig. 19 we compare the relative abundances [Ge/Sr] with [Sr/Eu] for the same sample used in Fig. 18, and one can find a marginal correlation between the Ge enhancement and the weakness of r-processing. The bottom panel in Fig. 19 compares the

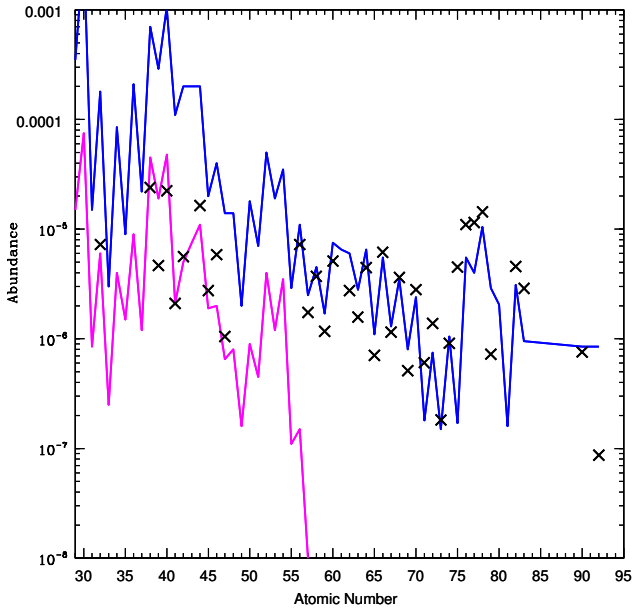

Fig. 17. Comparison of the observed abundances in CS 31082-001 (crosses) with yields from Farouqi et al. (2010), using Y_e of 0.498 (magenta solid line) and 0.482 (blue solid line). For each Y_e the superposition of the entropies spans from $S = 5\ k_B$/nucleon to the maximum entropy $S_{final}(Y_e) \sim 300\ k_B$/nucleon.

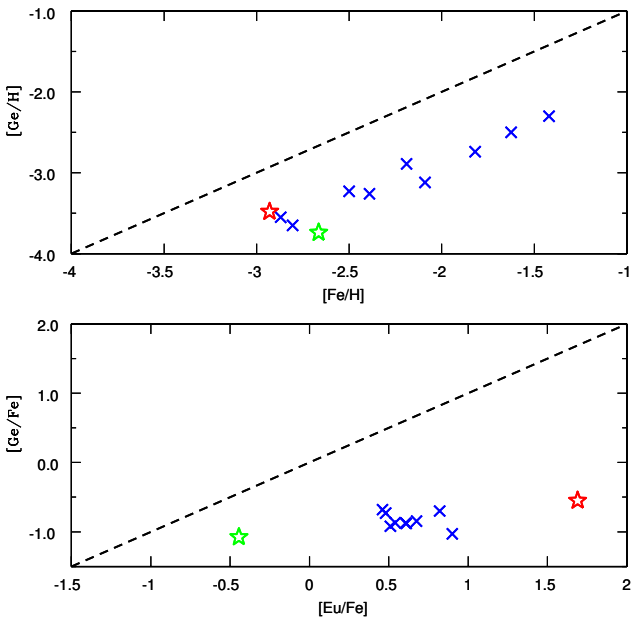

Fig. 18. Relative Ge abundances [Ge/H] displayed as a function of [Fe/H] (*top*) and the correlation between the abundance ratios [Ge/Fe] and [Eu/Fe] (*bottom*). The blue symbols represent the original data from Cowan et al. (2005); our new abundances for CS 31082-001 is marked as the red star. The r-poor HD 122563 is marked as the green star. The dashed line indicates the solar abundance ratio of these elements.

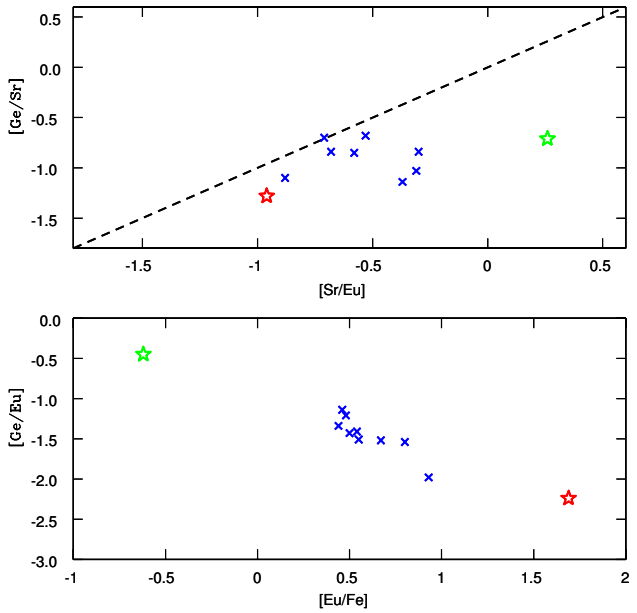

Fig. 19. Relative abundances [Ge/Sr] displayed as a function of [Sr/Eu] (*top*) and correlation between the abundance ratios [Ge/Eu] and [Eu/Fe] (*bottom*). Symbols as in Fig. 19.

Ge abundance to the level of heavy r-elements in the stars, represented by the Eu abundance, as a function of the enhancement in r-process elements. We find a clear anticorrelation between the r-process richness and the Ge enhancement. In fact, Fig. 17 shows that the low Ge abundance in our r-rich star CS 31082-001 is better described by the neutrino wind models, while the high Ge abundance in the r-poor star HD 122563 is explained well by the electron-capture supernova model (see Fig. 5 in Wanajo et al. 2011). This indicates that Ge serves as a key element in constraining the astrophysical conditions for r-process nucleosynthesis.

It is worth noting that the region between the iron peak and the first peak of the r-process is historically thought to be the beginning of the r-process, and Ge is at the end of the Fe peak. In fact, the noncorrelation between the Ge abundance and the general level of heavy r-elements (Fig. 18, bottom panel), as well as the anticorrelation between those (Fig. 19, bottom panel), leads us to not discard the possibility of an iron peak (or NSE) origin to Ge.

Using a sample of metal-poor stars from Cowan et al. (2005), François et al. (2007), Roederer et al. (2010b), Peterson (2011), and Hansen et al. (2012), we calculated the correlation between [X/Fe] with respect to [Eu/Fe], where X represents the elements available from the iron peak to the heavy r-elements. Figure 20 shows our results, representing the average behaviour in each group of elements; in the case of the iron peak the value was calculated without the result for germanium. One can see that the behaviour of germanium is not clear enough to allow us to decide about its origin, and we stress that it is necessary to collect more observational data and perform an NLTE analysis of this element to reach a firm conclusion.

5. Conclusions

We have determined the first abundances of molybdenum and germanium in CS 31082-001, using our STIS spectrum. In fact, there is a lack of stellar abundances of these elements for EMP stars compared to other elements from the first peak, so our new abundance determinations are particularly valuable, and should be viewed as part of a large project by several authors, trying to solve this observational gap in an attempt to understand the origin of the lightest trans-Fe elements.

Following the completion of the abundance analysis of this star, we have also derived new abundances for lutetium and tantalum, which agree with the solar system r-process abundance, confirming the consistency between the r-process in EMP stars and the solar system pattern, from Ba through the third r-process peak, which also confirms the universal behaviour of the process

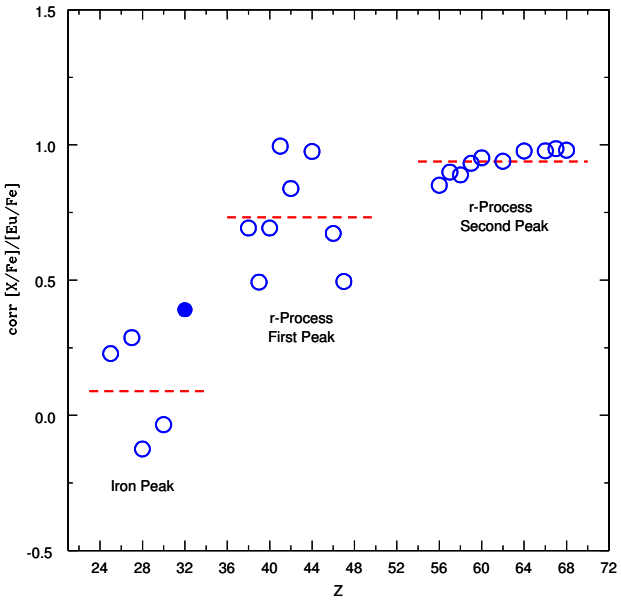

Fig. 20. Correlation between [X/Fe] with respect to [Eu/Fe] using a sample of metal-poor stars (see text). Germanium is represented as the filled circle. The dashed lines represent the average behaviour in each group of elements.

in this range of elements. On the other hand, this consistency does not extend to the lighter heavy elements or to the heaviest elements in the actinide region.

Furthermore, the HST/STIS spectra of CS 31082-001 have permitted us to make the first abundance determinations of W and Re in an EMP star. These two elements are extremely important for studying the transition region between the second and the third peaks of the r-process. Together with the previous abundances, our new results make CS 31082-001 the most thoroughly studied r-II object to date, and a major template for studies of r-process models, with a total of 37 detections of neutron-capture elements, superseding the previous record held by BD+17°3248.

The abundances of the second peak of CS 31082-001 are reasonably well represented by those of the cold model by Wanajo (2007), but not the abundances of the first peak. As in some cases, an additional production of the first-peak elements by other processes could be invoked. More elegantly, the model of Farouqi et al. with different electron abundances Y_e can explain the first (including Ge) and second peaks.

We also present the first NLTE+3D lead abundance in this star, which, together with the other heavy elements from the third peak, underscores that supernova neutrino wind models with lower temperatures satisfactorily describe the formation of the elements in this region. In general, the comparisons between calculations and observations argue for a combination of processes to reproduce the full range of observed stellar abundances.

A final question regards the origin of the extreme r-II stars, which, like CS 31082-001 itself, are generally single (Hansen et al. 2011). This suggests that the supernova models discussed as the astrophysical sites of the r-process need to consider not only the details of the supposed neutrino wind, but also the effects of non-spherical or jet-like explosions.

Acknowledgements. C.S. and B.B. acknowledge grants from CAPES, CNPq and FAPESP. M.S., V.H., B.P., R.C., F.S., P.B. and P.F. acknowledge the support of the CNRS (PNCG and PNPS). J.A. and B.N. acknowledge partial financial support from the Carlsberg Foundation and the Danish Natural Science Research Council. T.C.B. acknowledges partial funding of this work from grants PHY 02-16783 and PHY 08-22648: Physics Frontier Center/Joint Institute for Nuclear Astrophysics (JINA), awarded by the US National Science Foundation.

References

Alvarez, R., & Plez, B. 1998, A&A, 330, 1109
Anders, E., & Grevesse, N. 1989, Geochim. Cosmochim. Acta, 53, 197
Andrievsky, S. M., Spite, M., Korotin, S. A., et al. 2009, A&A, 494, 1083
Andrievsky, S. M., Spite, F., Korotin, S. A., et al. 2011, A&A, 530, A105
Anstee, S. D., & O'Mara, B. J. 1995, MNRAS, 276, 859
Arcones, A., & Montes, F. 2011, ApJ, 731, 5
Asplund, M., Gustafsson, B., Kiselman, D., et al. 1997, A&A, 318, 521
Asplund, M., Carlsson, M., & Botnen, A. V. 2003, A&A, 399, 31
Asplund, M., Grevesse, N., Sauval, A. J., et al. 2004, A&A, 417, 751
Asplund, M., Grevesse, N., Sauval, A. J., et al. 2009, ARA&A, 47, 481
Barbuy, B., Spite, M., Hill, V., et al. 2011, A&A, 534, A60
Barklem, P. S., & O'Mara, B. J. 1997, MNRAS, 290, 102
Barklem, P. S., O'Mara, B. J., & Ross, J. E. 1998, MNRAS, 296, 1057
Barklem, P. S., Belyaev, A. K., & Asplund, M. 2003, A&A, 409, 1
Beers, T. C., & Christlieb, N. 2005, ARA&A, 43, 531
Biémont, E., Grevesse, N., Hannaford, P., et al. 1981, ApJ, 248, 867
Biémont, E., Lynga, C., Li, Z. S., et al. 1999, MNRAS, 303, 721
Burbidge, E. M., Burbidge, G. R., Fowler, W. A., et al. 1957, Rev. Mod. Phys., 29, 547
Caffau, E., Ludwig, H.-G., Steffen, M., et al. 2011, Sol. Phys., 268, 255
Cayrel, R., Depagne, E., Spite, M., et al. 2004, A&A, 416, 1117
Cayrel, R., Steffen, M., Chand, H., et al. 2007, A&A, 473, 37
Clayton, D. D. 1968, Principles of Stellar Evolution and Nucleosynthesis (NewYork: McGraw-Hill)
Cowan, J. J., Sneden, C., Burles, S., et al. 2002, ApJ, 572, 861
Cowan, J. J., Sneden, C., Beers, T. C., et al. 2005, ApJ, 627, 238
Cowan, J. J., Roederer, I. U., Sneden, C., et al. 2011, in RR Lyrae Stars, Metal-Poor Stars, and the Galaxy, ed. A. McWilliam (Pasadena, CA: The Observatories of the Carnegie Institution of Washington), 223
Den Hartog, E. A., Wickliffe, M. E., & Lawler, J. E. 2002, ApJ, 141, 255
Den Hartog, E. A., Lawler, J. E., Sneden, C., et al. 2003, ApJ, 148, 543
Den Hartog, E. A., Lawler, J. E., Sneden, C., et al. 2006, ApJ, 167, 292
Farouqi, K., Kratz, K.-L., Pfeiffer, B., et al. 2010, ApJ, 712, 1359
Fedchak, J. A., Den Hartog, E. A., Lawler, J. E., et al. 2000, ApJ, 542, 1109
Fischer, T., Whitehouse, S. C., Mezzacappa, A., et al. 2010, A&A, 517, A80
Fivet, V., Palmeri, P., Quinet, P., et al. 2006, EPJD, 37, 29
François, P., Depagne, E., Hill, V., et al. 2007, A&A, 476, 935
Freiburghaus, C., Rosswog, S., & Thielemann, F.-K. 1999, ApJ, 525, L121
Freytag, B., Steffen, M., & Dorch, B. 2002, Astron. Nachr., 323, 213
Freytag, B., Steffen, M., Ludwig, H.-G., et al. 2012, J. Comput. Phys., 231, 919
Fröhlich, C., Martínez-Pinedo, G., Liebendörfer, M., et al. 2006, Phys. Rev. Lett., 96, 142502
Goriely, S. 1999, A&A, 342, 881
Goriely, S., Samyn, M., Pearson, J. M., et al. 2005, Nucl. Phys. A, 750, 425
Goriely, S., Bauswein, A., & Janka, H.-T. 2011, ApJ, 738, L32
Grevesse, N., & Sauval, J. 1998, SSRv, 85, 161
Gustafsson, B., Bell, R. A., Eriksson, K., et al. 1975, A&A, 42, 407
Gustafsson, B., Edvardsson, B., Eriksson, K., et al. 2003, in Stellar Atmosphere Modeling Werner, ASP Conf. Ser., 288, 331
Gustafsson, B., Edvardsson, B., Eriksson, K., et al. 2008, A&A, 486, 951
Hannaford, P., Lowe, R. M., Grevesse, N., et al. 1982, ApJ, 261, 736
Hansen, T., Andersen, J., Nordström, B., et al. 2011, ApJ, 743, L1
Hansen, C. J., Primas, F., Hartman, H., et al. 2012, A&A, 545, A31
Hartmann, D., Woosley, S. E., & El Eid, M. F. 1985, ApJ, 297, 837
Hill, V., Plez, B., & Cayrel, R., et al. 2002, A&A, 387, 560
Hoffman, R. D., Woosley, S. E., Fuller, G. M., et al. 1996, ApJ, 460, 478
Hüdepohl, L., Müller, B., Janka, H.-T., et al. 2010, Phys. Rev. Lett., 104, 251101
Ishimaru, Y., & Wanajo, S. 1999, ApJ, 511, 33
Käppeler, F., Beer, H., & Wisshak, K. 1989, Rep. Prog. Phys., 52, 945
Korobkin, O., Rosswog, S., Arcones, A., et al. 2012, MNRAS, 426, 1940
Kratz, K.-L., Farouqi, K., Pfeiffer, B., et al. 2007, ApJ, 662, 39
Kupka, F., Piskunov, N., Ryabchikova, T. A., et al. 1999, A&AS, 138, 119
Lattimer, J. M., Mackie, F., Ravenhall, D. G., et al. 1977, ApJ, 213, 225
Lawler, J. E., Bonvallet, G., & Sneden, C. 2001a, ApJ, 556, 452
Lawler, J. E., Wickliffe, M. E., Den Hartog, E. A., et al. 2001b, ApJ, 563, 1075
Lawler, J. E., Wickliffe, M. E., Cowley, C. R., et al. 2001c, ApJ, 137, 341
Lawler, J. E., Den Hartog, E. A., Sneden, C., et al. 2006, ApJ, 162, 227
Lawler, J. E., Den Hartog, E. A., Labby, Z. E., et al. 2007, ApJ, 169, 120
Lawler, J. E., Sneden, C., Cowan, J. J., et al. 2008, ApJ, 178, 71
Lawler, J. E., Sneden, C., Cowan, J. J., et al. 2009, ApJ, 182, 51
Ljung, G., Nilsson, H., Asplund, M., et al. 2006, A&A, 456, 1181
Lodders, K., Palme, H., & Gail, H.-P. 2009, Landolt-Börnstein – Group VI Astronomy and Astrophysics Numerical Data and Functional Relationships in Science and Technology Volume 4B: Solar System, ed. J. E. Trümper, 4.4., 44
Martínez-Pinedo, G., Fischer, T., Lohs, A., et al. 2012, Phys. Rev. Lett., 109, id. 251104

Mashonkina, L., Ryabtsev, A., & Frebel, A. 2012, A&A, 540, A98
Mathews, G. J., & Cowan, J. J. 1990, Nature, 345, 491
McWilliam, A. 1998, AJ, 115, 1640
Meyer, B. S. 1989, ApJ, 343, 254
Meyer, B. S., McLaughlin, G. C., & Fuller, G. M. 1998, Phys. Rev. C, 58, 3696
Nilsson, H., Engström, L., Lundberg, H., et al. 2008, EPJD, 49, 13
Palmeri, P., Quinet, P., Wyart, J.-F., et al. 2000, Phys. Scr., 61, 323
Peterson, R. C. 2011, ApJ, 742, 21
Peterson, R. C., Dorman, B., & Rood, R. T. 2001, ApJ, 559, 372
Plez, B., Brett, J. M., & Nordlund, A. 1992, A&A, 256, 551
Plez, B., Hill, V., Cayrel, R., et al. 2004, A&A, 428, L9
Pruet, J., Hoffman, R. D., Woosley, S. E., et al. 2006, ApJ, 644, 1028
Quinet, P., Palmeri, P., Biémont, E., et al. 1999, MNRAS, 307, 934
Roberts, L. F. 2012, ApJ, 755, 126
Roberts, L. F., Reddy, S., & Shen, G. 2012, Phys. Rev. C, 86, id. 065803
Roederer, I. U., Sneden, C., Lawler, J. E., et al. 2010a, ApJ, 714, L123
Roederer, I. U., Cowan, J. J., Karakas, A. I., et al. 2010b, ApJ, 724, 975
Sbordone, L., Bonifacio, P., Caffau, E., et al. 2010, A&A, 522, A26
Schatz, H., Toenjes, R., Pfeiffer, B., et al. 2002, ApJ, 579, 638
Sikström, C. M., Pihlemark, H., Nilsson, H., et al. 2001, J. Phys. B Atom. Mol. Phys., 34, 477
Simmerer, J., Sneden, C., Cowan, J. J., et al. 2004, ApJ, 617, 1091
Sneden, C. A. 1973, Ph.D. Thesis, The University of Texas at Austin
Sneden, C., Cowan, J. J., & Gallino, R. 2008, ARA&A, 46, 241
Sneden, C., Lawler, J. E., Cowan, J. J., et al. 2009, ApJ, 182, 80
Sobeck, J. S., Lawler, J. E., & Sneden, C. 2007, ApJ, 667, 1267
Spite, M., Cayrel, R., Plez, B., et al. 2005, A&A, 430, 655
Spite, M., Andrievsky, S. M., Spite, F., et al. 2012, A&A, 541, A143
Surman, R., McLaughlin, G. C., Ruffert, M., et al. 2008, ApJ, 679, L117
Thielemann, F.-K., Hirschi, R., Liebendörfer, M., et al. 2010, Lect. Not. Phys., 812, 153
Travaglio, C., Gallino, R., Arnone, E., et al. 2004, ApJ, 601, 864
Truran, J. W. 1981, A&A, 97, 391
Wanajo, S. 2006, ApJ, 647, 1323
Wanajo, S. 2007, ApJ, 666, L77
Wanajo, S., & Ishimaru, I. 2006, Nucl. Phys. A, 777, 676
Wanajo, S., & Janka, H.-T. 2012, ApJ, 746, 180
Wanajo, S., Itoh, N., Ishimaru, Y., et al. 2002, ApJ, 577, 853
Wanajo, S., Janka, H.-T., & Müller, B. 2011, ApJ, 726, 15
Wickliffe, M. E., Salih, S., & Lawler, J. E. 1994, J. Quant. Spec. Radiat. Transf., 51, 545
Wickliffe, M. E., & Lawler, J. E. 1997, J. Opt. Soc. Am. B, 14, 737
Woosley, S. E., & Hoffman, R. D. 1992, ApJ, 395, 202
Woosley, S. E., Wilson, J. R., Mathews, G. J., et al. 1994, ApJ, 433, 229
Zhiguo, Z., Li, Z. S., Lundberg, H., et al. 2000, J. Phys. B Atom. Mol. Phys., 33, 521

Pages 15 to 17 are available in the electronic edition of the journal at http://www.aanda.org

Appendix A: Line list and atomic data

Table A.1 presents the wavelengths, excitation potentials, and oscillator strengths, with references, of the lines of the neutron-capture elements that were used to derive the abundances discussed in the paper.

Table A.1. Spectral lines seen in CS 31082-001 and abundances obtained from our HST/STIS and VLT/UVES spectra.

λ (Å)	χ_{ex} (eV)	log gf	$A(X)_{STIS}$	$A(X)_{UVES}$	Ref.
		Ge I ($Z = 32$)			
3039.067	0.883	–0.040	0.10	–	1
		Y II ($Z = 39$)			
3200.272	0.130	–0.430	–	–0.08	2
3203.322	0.104	–0.370	–	–0.07	2
3216.682	0.130	–0.020	–	–0.27	2
3242.280	0.180	0.210	–	–0.10	2
3448.808	0.409	–1.440	–	–0.15	2
3549.005	0.130	–0.280	–	–0.12	2
3584.518	0.104	–0.410	–	–0.13	2
3600.741	0.180	0.280	–	–0.20	2
3601.919	0.104	–0.180	–	–0.18	2
3611.044	0.130	0.110	–	–0.23	2
3628.705	0.130	–0.710	–	–0.13	2
3633.122	0.000	–0.100	–	–0.25	2
3710.294	0.180	0.460	–	–0.11	2
3774.331	0.130	0.210	–	–0.14	2
3788.694	0.104	–0.070	–	–0.13	2
		Zr II ($Z = 40$)			
2699.593	0.039	–1.170	0.73	–	3
2732.711	0.095	–0.490	0.72	–	3
2758.792	0.000	–0.560	–0.07	–	3
2818.738	0.959	0.020	0.65	–	4
2915.973	0.466	–0.500	0.69	–	3
2916.625	0.359	–1.110	0.60	–	3
2952.236	0.164	–1.250	0.65	–	4
2962.673	0.359	–0.570	0.65	–	3
3019.832	0.039	–1.130	0.80	–	4
3028.045	0.972	0.020	0.45	–	4
3030.915	0.000	–1.040	0.66	0.60	4
3054.837	1.011	0.180	0.35	–	4
3061.334	0.095	–1.380	0.35	–	4
3095.073	0.039	–0.960	–	0.50	4
3125.926	0.000	–0.883	–	0.69	4
3129.763	0.039	–0.650	–	0.63	4
3133.489	0.959	–0.200	–	0.58	4
3138.683	0.095	–0.460	–	0.57	4
3231.692	0.039	–0.590	–	0.70	4
3241.042	0.039	–0.504	–	0.39	4
3272.221	0.000	–0.700	–	0.70	4
3279.266	0.095	–0.230	–	0.60	4
3284.703	0.000	–0.480	–	0.65	4
3305.153	0.039	–0.690	–	0.68	4
3314.488	0.713	–0.686	–	0.50	4
3334.607	0.559	–0.797	–	0.65	4
3338.414	0.959	–0.578	–	0.40	4
3340.574	0.164	–0.461	–	0.43	4
3356.088	0.095	–0.513	–	0.59	4
3357.264	0.000	–0.736	–	0.70	4
3391.982	0.164	0.463	–	0.70	4
3393.122	0.039	–0.700	–	0.60	4
3403.673	0.999	–0.576	–	0.45	4
3419.128	0.164	–1.574	–	0.50	4
3424.813	0.039	–1.305	–	0.62	4
3430.514	0.466	–0.164	–	0.54	4
3457.548	0.559	–0.530	–	0.68	4
3402.868	1.532	–0.330	–	0.55	4
3479.029	0.527	–0.690	–	0.58	5
3479.383	0.713	0.170	–	0.20	5
3499.560	0.409	–0.810	–	0.44	5
3505.682	0.164	–0.360	–	0.60	5
3506.048	1.236	–0.860	–	0.43	4
3520.869	0.559	–1.089	–	0.20	4
3525.803	0.359	–0.653	–	0.25	4
3536.935	0.359	–1.306	–	0.35	4
3551.939	0.095	–0.310	–	0.65	5
3556.585	0.466	0.140	–	0.00	4
3573.055	0.319	–1.041	–	0.63	4
3578.211	1.208	–0.607	–	0.52	4
3588.300	0.409	–1.130	–	0.60	5
3607.373	1.236	–0.640	–	0.35	5
3611.889	1.743	0.450	–	0.25	4
3613.102	0.039	–0.465	–	0.67	4
3614.765	0.359	–0.252	–	0.54	4
3630.004	0.359	–1.110	–	0.52	5
3636.436	0.466	–1.035	–	0.52	4
3674.696	0.319	–0.446	–	0.30	4
3714.794	0.527	–0.930	–	0.72	5
3766.795	0.409	–0.812	–	0.67	4
		Nb II ($Z = 41$)			
2876.957	0.439	–0.490	–0.62	–	4
2908.237	0.292	–0.340	–0.62	–	4
2910.581	0.376	–0.190	–0.70	–	4
2911.738	0.326	–0.270	–0.62	–	4
2950.878	0.514	0.210	–0.50	–	4
2994.718	0.514	–0.250	–0.15	–	4
3028.433	0.439	–0.410	–0.38	–0.27	4
3191.093	0.514	–0.260	–	–0.55	4
3215.591	0.439	–0.190	–	–0.58	4
		Mo II ($Z = 42$)			
2660.576	1.492	–0.136	–0.15	–	6
2871.507	1.540	0.056	–0.26	–	6
2930.485	1.492	–0.228	0.08	–	6
		Ru I ($Z = 44$)			
2874.988	0.000	–0.240	0.65	–	7
3436.736	0.148	0.015	–	0.45	7
3498.942	0.000	0.310	–	0.27	7
3728.025	0.000	0.270	–	0.35	7
		Rh I ($Z = 45$)			
3396.819	0.000	0.050	–	–0.45	4
3434.885	0.000	0.450	–	–0.41	4
3700.907	0.190	–0.100	–	–0.40	4
		Pd I ($Z = 46$)			
3242.700	0.814	–0.070	–	–0.10	4
3404.579	0.814	0.320	–	–0.18	4
3516.944	0.962	–0.240	–	–0.07	4
3634.690	0.814	0.090	–	–0.02	4
		Ag I ($Z = 47$)			
3280.679	0.000	–0.050	–	–1.03	4
3382.889	0.000	–0.377	–	–0.65	4
		Ce II ($Z = 58$)			
3263.885	0.459	–0.390	–	–0.40	4
3426.205	0.122	–0.660	–	–0.38	8
3507.941	0.175	–0.960	–	–0.27	8
3520.520	0.175	–0.910	–	–0.32	8
3534.045	0.521	–0.140	–	–0.30	8
3539.079	0.320	–0.270	–	–0.29	8
3577.456	0.470	0.140	–	–0.30	8
3659.225	0.175	–0.670	–	–0.38	8
3709.929	0.122	–0.260	–	–0.20	8
3781.616	0.529	–0.260	–	–0.22	8
		Nd II ($Z = 60$)			
3285.085	0.000	–1.050	–	–0.08	4

Table A.1. continued.

λ (Å)	χ_{ex} (eV)	log gf	$A(X)_{STIS}$	$A(X)_{UVES}$	Ref.
3300.143	0.000	–1.036	–	–0.30	4
3325.889	0.064	–1.174	–	–0.20	4
3334.465	0.182	–0.930	–	–0.22	9
3555.764	0.321	–0.950	–	–0.30	9
3560.718	0.471	–0.500	–	–0.38	9
3598.021	0.064	–1.020	–	–0.22	9
3609.780	0.000	–0.800	–	–0.25	9
3730.577	0.380	–0.611	–	–0.15	4
3738.055	0.559	–0.040	–	–0.21	9
3741.424	0.064	–0.680	–	–0.15	9
3763.472	0.205	–0.430	–	–0.20	9
3779.462	0.182	–0.560	–	–0.26	9
3780.382	0.471	–0.350	–	–0.28	9
3784.245	0.380	0.150	–	–0.13	9
3795.454	0.205	–0.650	–	–0.21	9
3803.471	0.205	–0.390	–	–0.20	9
3808.767	0.064	–0.650	–	–0.12	9
		Sm II ($Z = 62$)			
3218.596	0.185	–0.640	–	–0.53	10
3244.686	0.185	–1.330	–	–0.45	10
3253.403	0.104	–0.770	–	–0.55	10
3304.517	0.000	–1.190	–	–0.45	4
3307.027	0.659	–0.301	–	–0.15	4
3321.189	0.378	–0.362	–	–0.43	4
3384.654	0.378	–0.741	–	–0.32	4
3568.271	0.485	0.290	–	–0.35	10
3583.372	0.185	–1.110	–	–0.27	10
3604.281	0.485	–0.030	–	–0.38	10
3609.492	0.277	0.160	–	–0.45	10
3621.210	0.104	–0.510	–	–0.46	10
3627.004	0.277	–0.510	–	–0.48	10
3661.352	0.041	–0.360	–	–0.45	10
3670.821	0.104	–0.240	–	–0.58	10
3706.752	0.485	–0.600	–	–0.50	10
3718.883	0.378	–0.310	–	–0.35	10
3731.263	0.104	–0.330	–	–0.70	10
3739.120	0.041	–0.430	–	–0.45	10
3743.877	0.333	–0.550	–	–0.21	10
3758.460	0.000	–1.102	–	–0.30	4
3760.710	0.185	–0.400	–	–0.48	10
3762.588	0.248	–0.850	–	–0.43	10
		Eu II ($Z = 63$)			
2906.669	0.000	–0.440	–0.75	–	11
		Gd II ($Z = 64$)			
2833.748	0.492	–0.096	–0.22	–	4
3358.625	0.032	0.250	–	–0.32	12
3360.712	0.032	–0.540	–	–0.33	12
3362.239	0.079	0.430	–	–0.30	12
3364.245	0.000	–1.086	–	–0.35	4
3392.527	0.079	–0.330	–	–0.25	12
3418.729	0.000	–0.360	–	–0.22	12
3422.464	0.240	0.710	–	–0.06	12
3423.924	0.000	–0.550	–	–0.34	12
3439.208	0.382	0.080	–	–0.36	12
3439.787	0.425	–0.120	–	–0.28	12
3439.988	0.240	0.210	–	–0.24	12
3451.236	0.382	–0.260	–	–0.32	12
3454.907	0.032	–0.640	–	–0.29	12
3463.990	0.427	0.250	–	–0.32	12
3467.274	0.425	0.080	–	–0.39	12
3473.224	0.032	–0.370	–	–0.23	12
3481.802	0.492	0.110	–	–0.35	12
3482.607	0.427	–0.470	–	–0.35	12
3491.960	0.000	–0.530	–	–0.25	12
3557.058	0.600	0.040	–	–0.28	12
3646.196	0.240	0.320	–	–0.39	12

Table A.1. continued.

λ (Å)	χ_{ex} (eV)	log gf	$A(X)_{STIS}$	$A(X)_{UVES}$	Ref.
3654.624	0.079	–0.080	–	–0.27	12
3656.152	0.144	–0.020	–	–0.36	12
3671.205	0.079	–0.220	–	–0.25	12
3699.737	0.354	–0.290	–	–0.37	12
3768.396	0.079	0.210	–	–0.25	12
3796.384	0.032	0.020	–	–0.22	12
		Tb II ($Z = 65$)			
2934.802	0.126	–0.596	–0.50	–	4
3509.144	0.000	0.700	–	–1.05	13
3633.287	0.641	0.090	–	–1.00	13
3641.655	0.649	0.040	–	–1.00	13
		Dy II ($Z = 66$)			
3407.796	0.000	0.180	–	–0.15	14
3413.784	0.103	–0.520	–	–0.16	14
3434.369	0.000	–0.450	–	–0.19	14
3454.317	0.103	–0.140	–	–0.16	14
3456.559	0.590	–0.110	–	–0.12	14
3460.969	0.000	–0.070	–	–0.14	14
3531.707	0.000	0.770	–	+0.15	14
3534.960	0.103	–0.040	–	–0.09	14
3536.019	0.538	0.530	–	–0.18	14
3546.832	0.103	–0.550	–	–0.11	14
3550.218	0.590	0.270	–	–0.22	14
3563.148	0.103	–0.360	–	–0.11	14
3694.810	0.103	–0.110	–	–0.08	14
		Er II ($Z = 68$)			
2897.518	1.654	0.573	–0.20	–	4
2904.468	0.846	0.330	–0.10	–	15
2964.520	0.846	0.580	–0.30	–	15
3364.076	0.055	–0.420	–	–0.40	15
3441.130	0.055	–0.580	–	–0.30	15
3499.103	0.055	0.290	–	–0.40	15
3524.913	0.000	–0.790	–	–0.40	15
3549.844	0.670	–0.290	–	–0.36	15
3559.894	0.000	–0.690	–	–0.45	15
3580.518	0.055	–0.620	–	–0.35	15
3616.566	0.000	–0.310	–	–0.14	15
3618.916	0.670	–0.500	–	–0.12	15
3633.536	0.000	–0.530	–	–0.46	15
3700.720	0.055	–1.290	–	–0.22	4
3729.524	0.000	–0.590	–	–0.29	15
3742.640	0.636	–0.360	–	–0.36	15
3786.836	0.000	–0.520	–	–0.34	15
		Tm II ($Z = 69$)			
3015.294	0.029	–0.590	–1.00	–	16
3131.255	0.000	0.080	–	–1.25	16
3362.615	0.029	–0.200	–	–1.00	16
3397.498	0.000	–0.810	–	–1.11	16
3462.197	0.000	0.030	–	–1.31	14
3700.256	0.029	–0.380	–	–1.18	14
3701.363	0.000	–0.540	–	–1.29	14
3761.914	0.000	–0.450	–	–1.22	16
3795.760	0.029	–0.230	–	–1.22	14
		Lu II ($Z = 71$)			
2847.505	1.463	–0.230	–1.03	–	17
2963.318	1.463	–0.240	–1.00	–	17
3077.605	1.542	0.160	–	–1.20	17
		Hf II ($Z = 72$)			
3012.900	0.000	–0.600	–0.77	–	18
3109.113	0.787	–0.260	–	–0.60	18
3255.279	0.452	–1.210	–	–0.55	18
3399.793	0.000	–0.570	–	–0.81	18
3569.034	0.787	–0.460	–	–0.90	18
		Ta II ($Z = 73$)			
2635.583	0.128	0.700	–2.15	–	4
2832.702	0.847	–0.070	–1.05	–	4

Table A.1. continued.

λ (Å)	χ_{ex} (eV)	log gf	$A(X)_{STIS}$	$A(X)_{UVES}$	Ref.
		W II ($Z = 74$)			
2697.706	0.188	–0.870	–0.90	–	4
		Re I ($Z = 75$)			
2930.613	1.867	2.000	–0.20	–	4
		Re II ($Z = 75$)			
2637.006	2.373	1.020	–0.21	–	4

References. (1) Biémont et al. (1999); (2) Hannaford et al. (1982); (3) Ljung et al. (2006); (4) VALD; (5) Biémont et al. (1981); (6) Sikström et al. (2001); (7) Wickliffe et al. (1994); (8) Lawler et al. (2009); (9) Den Hartog et al. (2003); (10) Lawler et al. (2006); (11) Zhiguo et al. (2000); (12) Den Hartog et al. (2006); (13) Lawler et al. (2001c); (14) Sneden et al. (2009); (15) Lawler et al. (2008); (16) Wickliffe & Lawler (1997); (17) Quinet et al. (1999); (18) Lawler et al. (2007).